The metamorphism and exhumation of the Himalayan metamorphic core, eastern Garhwal region, India

Christopher J. Spencer,[1,2] Ron A. Harris,[1] and Michael J. Dorais[1]

Received 4 December 2010; revised 30 November 2011; accepted 30 November 2011; published 4 February 2012.

[1] Geothermobarometric together with micro- and macro-structural data indicate ductile flow in the metamorphic core of the Himalaya in the Garhwal region of India. Peak metamorphic pressure and temperature increase dramatically across the Main Central Thrust (MCT) from ~5 kbar and ~550°C in the Lesser Himalayan Crystalline Sequence (LHCS) to ~14 kbar and ~850°C at ~3 km above the MCT in the Greater Himalayan Sequence (GHS). Pressures within the GHS then decrease upsection to ~8 kbar while temperatures remain nearly constant at ~850°C up to the structurally overlying South Tibetan Detachment (STD). The GHS exhibits sheath fold geometries are indicative of high degrees of ductile flow. Overprinting ductile structures are two populations of extensional conjugate fractures and normal faults oriented both parallel and perpendicular to the orogen. These fractures crosscut major tectonic boundaries in the region such as the MCT and STD, and are found throughout the LHCS, GHS, and Tethyan Sedimentary Sequence (TSS). The thermobarometric and metamorphic observations are consistent with a form of channel flow. However, channel flow does not account for exhumational structures that formed above the brittle-ductile transition. To explain all of the features seen in the metamorphic core of the Garhwal region of the Himalaya, both the theories of channel flow and critical taper must be taken into account. Channel flow can explain the exhumation of the GHS from the middle crust to the brittle-ductile transition. The most recent extensional deformation is consistent with a supercritical wedge.

Citation: Spencer, C. J., R. A. Harris, and M. J. Dorais (2012), The metamorphism and exhumation of the Himalayan metamorphic core, eastern Garhwal region, India, *Tectonics*, *31*, TC1007, doi:10.1029/2010TC002853.

1. Introduction

[2] The metamorphic core of the Himalayan Orogen found in the Eastern Garhwal region of northwest India consists of ~26 km thick sequence of amphibolite to granulite facies metasedimentary rocks known as the LHCS and the GHS [*Virdi*, 1986] (Figure 1). The Munsiari Formation (LHCS) structurally overlies the unmetamorphosed Mandhali Formation of the Lesser Himalayan Sequence along the Munsiari Thrust. The GHS structurally overlies the Munsiari Formation via the MCT (Figure 1). The STD juxtaposes the unmetamorphosed TSS down to the northeast over the high-grade metamorphic rocks of the GHS [*Virdi*, 1986; *Gururajan and Choudhuri*, 1999].

[3] The GHS represents the highest temperature rocks found in the Himalayan orogen south of the the Indus-Tsangpo Suture zone, and therefore is key to understanding the metamorphic evolution and degree of exhumation within the orogen [*Kohn et al.*, 2005]. This 5 to 30 km thick package of medium to high grade metasedimentary rocks extends nearly 2500 km (Figure 1a) along the strike of the Himalayan Orogen [*Jessup et al.*, 2008; *Yin*, 2006, and references therein]. Exhumation of the GHS in the Garhwal region is associated with southwestward directed thrust-sense shear along the MCT, focused erosion at the denudational front, and northeastward directed normal-sense shear along the STD. The STD has been variously interpreted as a passive roof thrust that allows for the extrusion of a tectonic wedge [*Webb et al.*, 2007], a system of normal faults that accommodate the orogenic taper associated with a supercritical wedge [*Robinson et al.*, 2006], or the upper boundary of a long-lasting channel flow that is causing the extrusion of the GHS from the high-grade metamorphosed Indian basement beneath southern Tibet [*Beaumont et al.*, 2004; *Jamieson et al.*, 2004].

[4] Various mechanisms proposed for the exhumation of the Himalayan metamorphic core are the focus of many empirical studies [e.g., *Carosi et al.*, 2006; *Robinson and Pearson*, 2006; *Cottle et al.*, 2007; *Kohn*, 2008; *Jessup et al.*, 2008; *Long and McQuarrie*, 2010]; numerical thermal-mechanical models are also employed to explain exhumation

[1]Department of Geological Sciences, Brigham Young University, Provo, Utah, USA.
[2]Department of Earth Sciences, University of St Andrews, St Andrews, UK.

0278-7407/12/2010TC002853

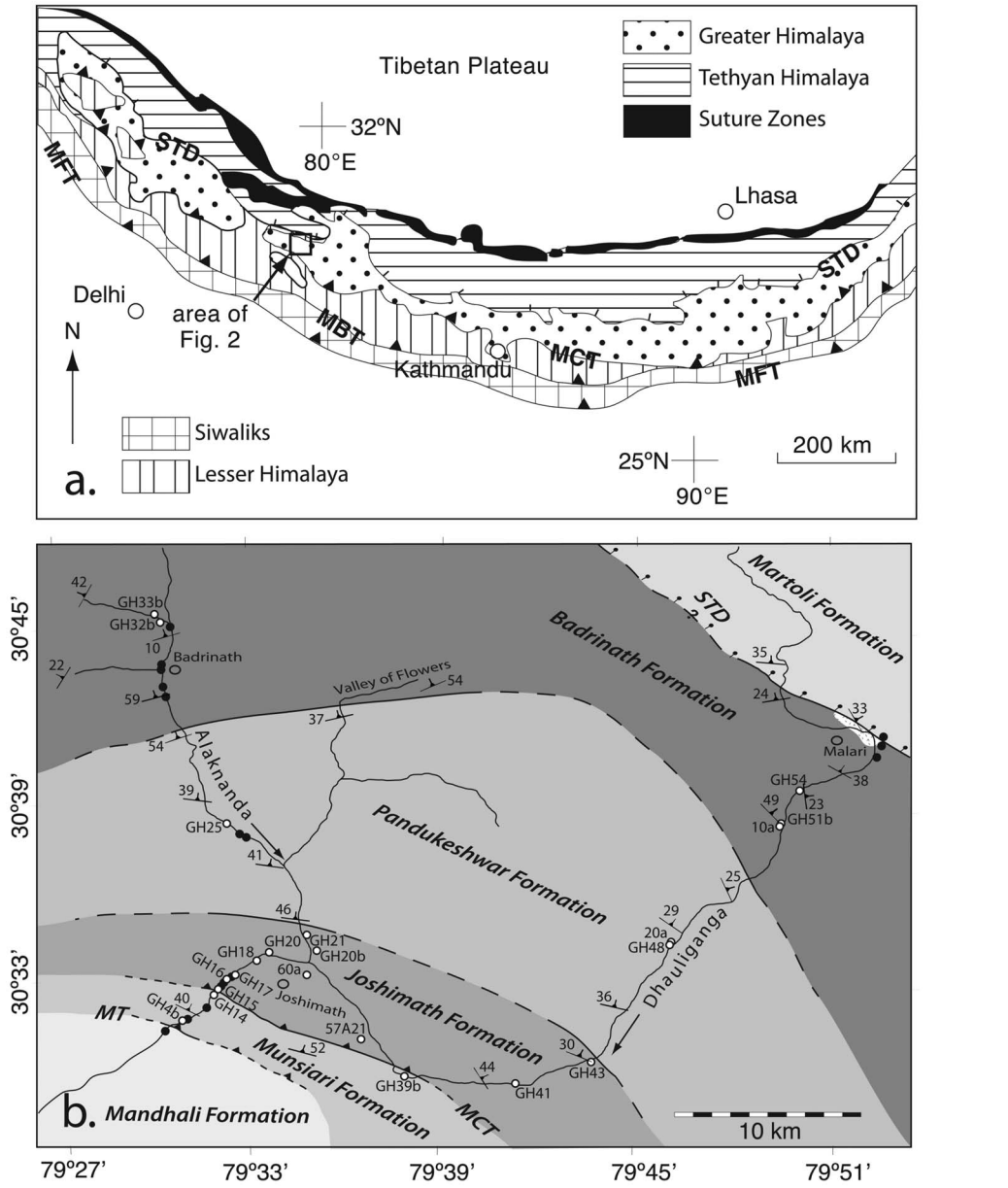

Figure 1. (a) Generalized tectonic map of the Himalayan orogen after *Ahmad et al.* [2000]. Major bounding structures include the South Tibetan Detachment (STD), Main Central Thrust (MCT), Main Boundary Thrust (MBT), and the Main Frontal Thrust (MFT). Study area shown in box. (b) Simplified geologic map [after *Virdi*, 1986; *Valdiya et al.*, 1999]. Locations of samples used for thermobarometry shown in open circles whereas sample used only for quartz thermometry are shown in black circles.

mechanisms [*Beaumont et al.*, 2001, 2004, 2006; *Jamieson et al.*, 2004; *Célérier et al.*, 2009b]. However, there are only a few detailed investigations of exhumation mechanisms of the GHS and they rarely integrate thermobarometry, phase equilibria, and geochronology with detailed structural measurements.

[5] This study investigates the peak metamorphic conditions and deformation mechanisms associated with the exhumation of the GHS in the Eastern Garhwal region of India (Figure 1b) by integrating structural field mapping and thermobarometry along two transects that follow the drainages of the Alaknanda and Dhauliganga. These rivers were chosen because they cross the GHS nearly perpendicular to the strike of the range and provide some of the greatest vertical structural relief through the range (~5 km of relief). A thermobarometric study along the same transects of this study was conducted by *Hodges and Silverberg* [1988]. However, phase equilibria constraints of *Kohn* [2008] and *Holland and Powell* [1998] show mineral assemblages in nine of the eleven samples used for this study violate phase equilibria constraints. Mineral compositions used to calculate pressure and temperature conditions did not

equilibrate at peak conditions [*Kohn*, 2008]. West of the study area, *Metcalfe* [1993] also reported pressures and temperatures from the Munsiari Formation and the GHS. However, the mineral assemblages reported from the upper half of the GHS also violate phase equilibria (see section 5). Futhermore, neither of these previous studies include a structural analysis.

2. Tectonostratigraphy

[6] The crystalline rocks of the Eastern Garhwal region along the studied transects are divided in two lithotectonic suites (Figure 2): (1) the Munsiari Formation of the LHCS and (2) the GHS (or Vaikrita Formation after *Gururajan and Choudhuri* [1999]). Overlying the GHS is the unmetamorphosed Martoli Formation (basal portion of TSS).

2.1. Munsiari Formation

[7] The Munsiari Formation (LHCS) includes garnet-bearing mica schists, calc-silicate lenses, and quartzite [*Gururajan and Choudhuri*, 1999]. Pelitic samples within the Munsiari Formation have quartz + biotite + plagioclase + garnet ± staurolite ± muscovite ± graphite ± andalusite. Garnet within the Munsiari Formation is synkinematic to the dominant foliation near the rim with early stage schistosity near the core (Figure 2a). At the base of the Munsiari Formation is the Munsiari Thrust, which places the Munsiari Formation on top of the unmetamorphosed Mandhali Formation of the Lesser Himalayan Sequence [*Valdiya*, 1980]. *Célérier et al.* [2009b] report an average white mica $^{40}Ar/^{39}Ar$ cooling age of 8.5 Ma for the Munsiari Formation.

2.2. MCT (Vaikrita Thrust)

[8] The MCT in the Eastern Garhwal region is defined as the ductile shear zone between the micaceous quartzites and chlorite-biotite schists of the Munsiari Formation and the kyanite gneisses of the Joshimath Formation of the GHS (Figure 1b) [*Valdiya*, 1978, 1980]. This also coincides with the Nd-isotopic boundary between the GHS and the LHCS defined by *Ahmad et al.* [2000]. Mylonitization is pervasive for tens of meters above and below the MCT [*Valdiya*, 1980]. No brittle structures are observed in association with the MCT.

2.3. GHS

[9] Within the Eastern Garhwal region, the GHS is divided in three formations [*Valdiya*, 1979, 1989]: a lower kyanite-bearing gneiss (Joshimath Formation); a thick micaceous meta-arkose (Pandukeshwar Formation); and an upper sillimanite-bearing augen gneiss (Badrinath Formation). The augens in the gneisses consist of quartz and feldspar porphyoclasts. The dominant foliation (S1) throughout the GHS is defined by aligned mica (biotite and muscovite) and is generally isoclinally folded (F1). A secondary foliation (S2) is locally developed in the hinge zone of F1 and is axial planar to isoclinal folds. Fold asymmetry is top-up-to-the-southwest in most of the GHS and top-down-to-the-northeast in the upper Badrinath Formation (Figure 6).

[10] The Joshimath Formation is a series of pelitic gneisses with schistose interlayers and have a mineral assemblage of quartz + biotite + plagioclase + garnet ± staurolite ± muscovite ± kyanite ± chlorite ± calcite ± graphite ± titanite ± opaques (rutile, ilmenite). At the base of the Joshimath Formation is the MCT. The top of the Joshimath Formation grades from metapelites to meta-arkose Pandukeshwar Formation. Farther to the east, *Paul* [1998] reported migmatites in the upper portion of the Joshimath Formation.

[11] The Pandukeshwar Formation consists mostly of meta-arkose and quartzite that transitions upward from the metapelites of the Joshimath Formation. The meta-arkose is primarily medium- to fine-grained and is interlayered with centimeter-scale bands of kyanite-bearing schist [*Paul*, 1998]. The lesser deformed arkose layers preserve both inverted and right-side-up cross beds. These depositional features demonstrate that large sections of the Pandukeshwar Formation are overturned by isoclinal folds. Mineral assemblages in this formation include quartz + K-feldspar ± plagioclase ± muscovite ± biotite ± garnet ± chlorite ± opaques (rutile, ilmenite, Cr-rich spinel).

[12] The Badrinath Formation primarily consists of migmatitic metapelites and calc-silicates that grade upward from the meta-arkose of the Pandukeshwar Formation. The Badrinath Formation is bounded at the top by the STD and structurally overlain by the unmetamorphosed Martoli Formation of the Tethyan Sedimentary Series. The metapelites of the Badrinath Formation have a similar mineral assemblage to the Joshimath Formation with the addition of sillimanite (quartz + biotite + plagioclase + garnet ± staurolite ± muscovite ± kyanite ± sillimanite ± cordierite ± chlorite ± calcite ± graphite ± rutile ± ilmenite) [*Paul*, 1998]. Calc-silicate layers generally contain calcite + diopside + quartz ± hornblende ± biotite ± scapolite ± actinolite ± tremolite [*Paul*, 1998]. Migmatitization of the Badrinath Formation occurs roughly 16 km up structural section from the MCT and increases upward to the STD. Migmatite stringers coalese in the upper Badrinath Formation where large Miocene-age leucogranite bodies intrude the surrounding metasediments. The leucogranite bodies consist of quartz + K-feldspar + plagioclase + muscovite ± biotite ± garnet ± tourmaline ± sericite (secondary) ± chlorite (secondary).

[13] The Badrinath and Joshimath Formations are similar enough that they are interpreted by *Virdi* [1986] as limbs of a large kilometer-scale isoclinal folds. However, this hypothesis predicts that the highest grade of metamorphism should be exposed in the core of the anticline, which is contrary to our observations of the highest grade rocks in the uppermost Badrinath Formation. The same relationship is also found to the east in the Kumaun region [*Paul*, 1998].

2.4. Martoli Formation (TSS)

[14] The Martoli Formation consists primarily of unmetamorphosed Cambrian age greywacke, sandstone, and shale [*Kacker and Srivastava*, 1996; *Valdiya et al.*, 1999]. This formation is juxtaposed against the GHS by the brittle north-dipping STD normal fault. This normal fault bounds the uppermost portion of the STD zone which consists of a 1–2 km wide ductile shear zone found throughout the Himalayas [*Burchfiel et al.*, 1992]. The STD is parallel to sub-parallel to the dominant foliation of the underlying Badrinath Formation dipping at ~30–40° (Figure 2). The bedding surfaces of the Martoli Formation are crosscut by

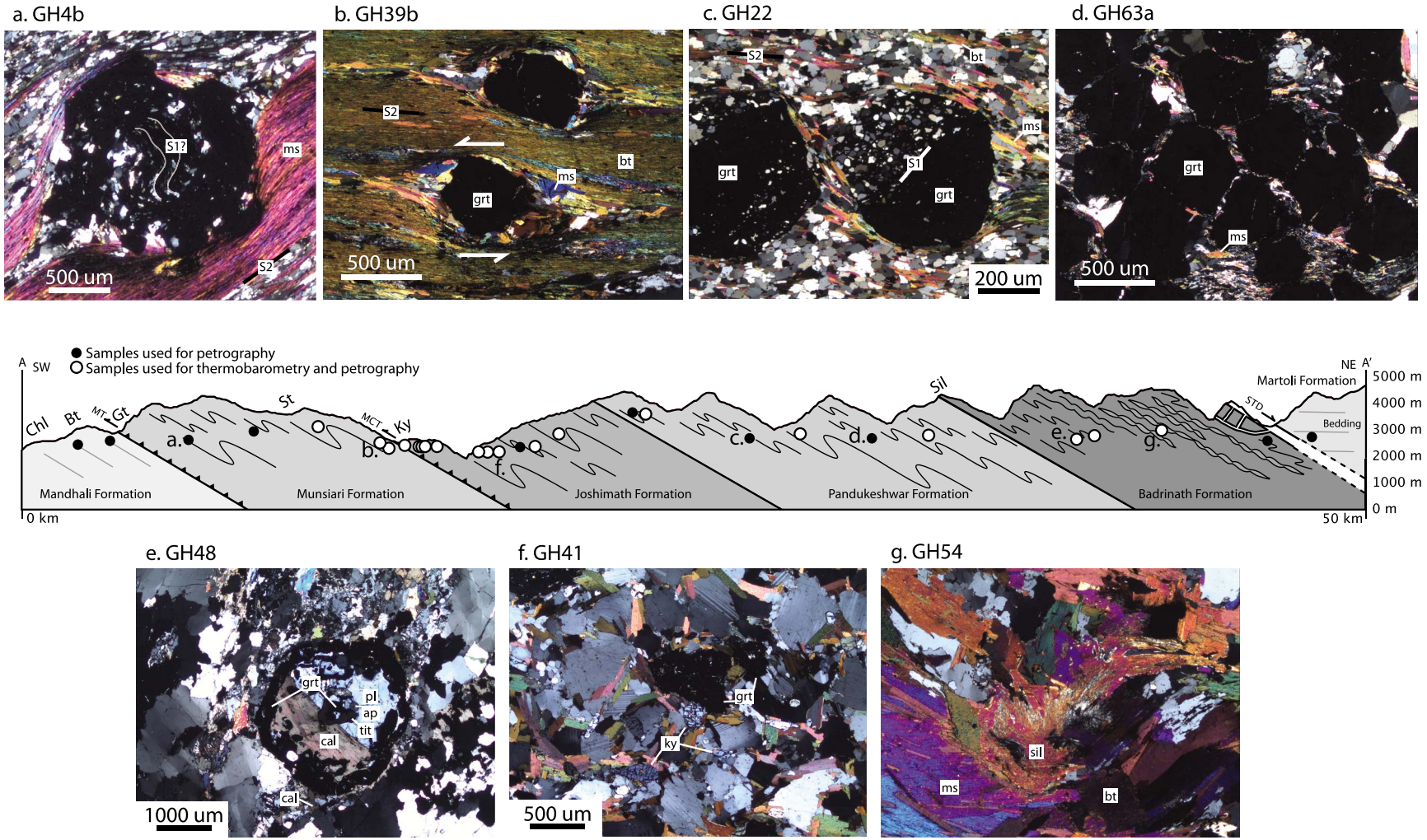

Figure 2. Simplified geological cross-section of the Alaknanda/Dhauliganga transect with approximate sample locations and photomicrographs of representative microstructures and mineral assemblages for various samples throughout the transects. All photomicrographs are crossed polars. (a) Garnet-bearing schist from the Munsiari Formation. Inclusions within garnet define contorted S1. (b) Garnet-bearing schist from the Munsiari Formation. Sense of shear is top-to-southwest with well developed sigma-tails surrounding garnets. (c) Garnet-bearing quartzite from the Pandukeshwar Formation. Inclusion rich portions of garnets delineate former quartz-rich zones whereas inclusion poor areas represent former clay-rich zones. The plane between these zones define S1. (d) Garnetite vien from the Pandukeshwar Formation. Garnet makes up nearly 80 modal percent confined within 3 cm layer parallel to dominant foliation. (e) Atoll garnet in the Badrinath Formation. The thin garnet rim surrounds calcite and plagioclase with smaller garnet, titanite and apatite inclusions. (f) Kyanite-garnet gneiss with plagioclase, muscovite, and biotite in the Joshimath Formation. (g) Sillimanite bearing gneiss the Badrinath Formation. Sillimanite forms fibrous clots. Muscovite is secondary and grew during retrograde metamorphism.

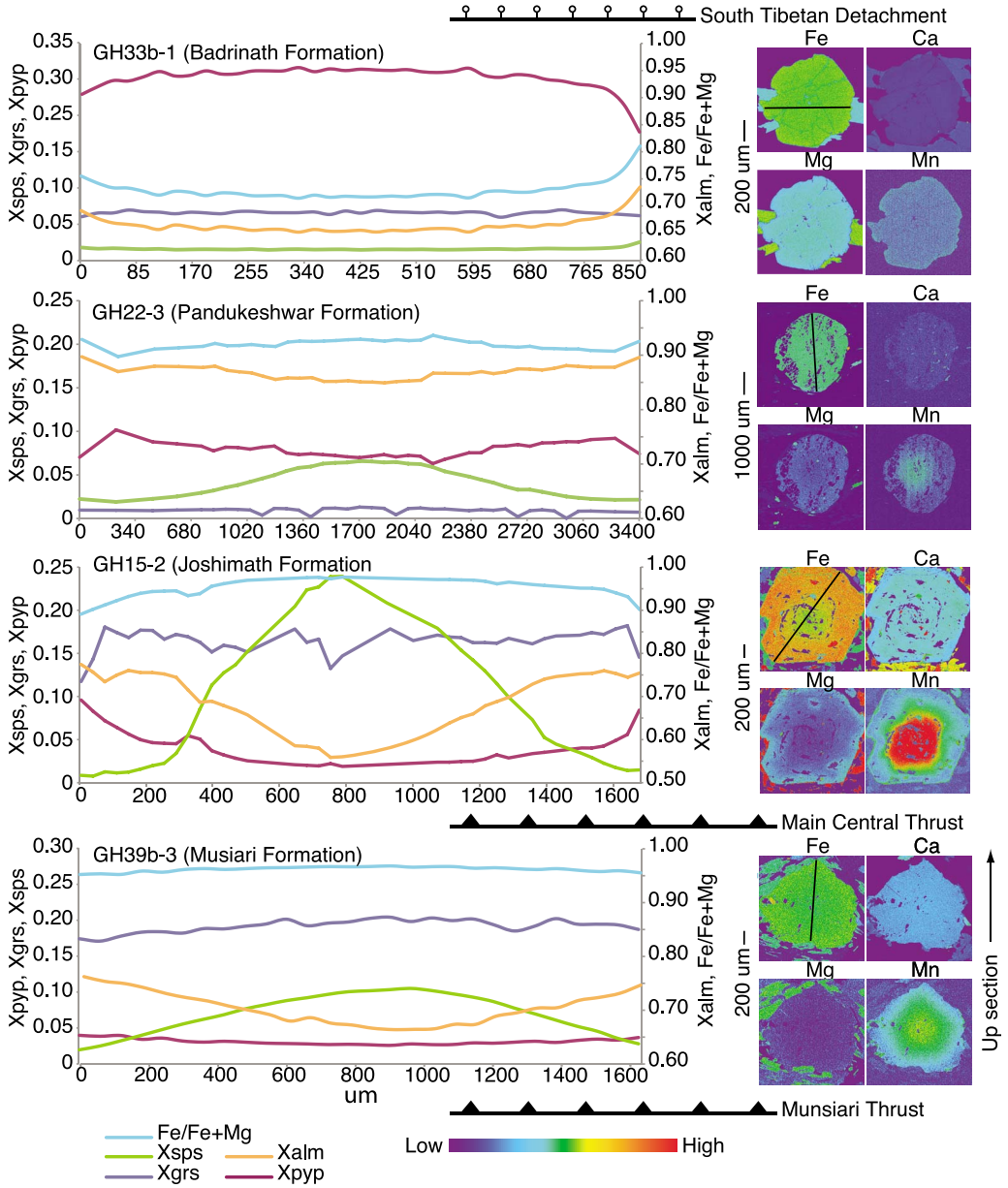

Figure 3. Representative compositional transects across garnet porphyoblasts. Mn profiles become increasingly homogenized up section. See text for explanation.

the steeper dipping STD. West of the studied section, *Metcalfe* [1993] described the same relationship between the upper GHS and the Martoli Formation. The Martoli Formation also features northeast verging cylindrical folds [*Kanungo and Murthy*, 1981].

3. Analytical Methods

[15] Twenty-one samples were selected for detailed thermobarometric analysis based upon the mineral assemblages necessary to constrain peak metamorphic conditions across the GHS. Thin sections were cut perpendicular to the dominant foliation and parallel to mineral lineation where observed. Electron microprobe analyses and X-ray compositional maps were made by using the Cameca SX-50 at the Department of Geological Sciences, Brigham Young University. Backscatter electron images and element maps of Fe, Mg, Ca, Mn were made of the phases selected for probe analyses. X-ray maps were used to determine appropriate locations for analyses and were collected with an acceleration voltage of 15kV, a current of 40 nA, and a time per pixel of 20 ms. Point analyses and/or transects were conducted across garnet, biotite, muscovite, and plagioclase to further characterize compositional zoning and to find appropriate areas for thermobarometric calculations. The analytical conditions used for quantitative analyses of silicates were 15 kV acceleration voltage, 20 s count time,

and 10–20 nA current. Natural minerals were used as standards to calibrate compositions of unknown minerals.

4. Metamorphic Textures and Compositional Zoning

[16] Complete records of electron microprobe analyses of various minerals and compositional maps used in this study are found in the auxiliary material.[1]

4.1. Munsiari Formation (LHCS)

[17] Garnet porphyroblasts in the Munsiari Formation typically have sieve textures dominated by quartz inclusions. Sieve garnets are confined to distinct quartz-rich and mica-poor domains whereas euhedral garnets are found in mica-rich domains. Most euhedral garnets have inclusion-rich cores and inclusion-free rims. Two different types of inclusion patterns are found: (1) sigmoidal inclusion trails oblique to the dominant foliation together with spiral inclusion trails or "snowball" garnets (Figure 2a); (2) syn-kinematic microstructures with muscovite fish and quartz porphyoclast σ-type porphyroclasts defining a top-to-the-southwest sense of shear (Figure 2b). Some samples also preserve post-kinematic muscovite that is randomly oriented and overgrows the dominant foliation.

[18] Compositional maps and point transects of garnet porphyroblasts (sample GH4b-4) (Figure 3) show Fe concentration increases or ocillates slightly from core (Xalm = 0.72) to rim (Xalm = 0.80), Ca is depleted in the core (Xgrs = 0.08) and oscillatory with a slight increase at the rim (Xgrs = 0.10), Mg is relatively homogeneous (Xpyr = 0.07 average), and Mn decreases from core (Xsps = 0.13) to rim (Xsps = 0.04). These bell-shaped chemical zoning profiles are characteristic of growth zoning that has remained unaltered by subsequent diffusion. In anhedral and sieve garnets the growth zoning is truncated along anhedral surfaces. However, there is no evidence for retrograde exchange reactions (Figure 3).

4.2. Joshimath Formation (Lower GHS)

[19] Most of the garnet porphyroblasts in the Joshimath Formation are petrographically similar to those found in the Munsiari Formation. Garnets in a representative sample from the Joshimath Formation (GH15–2) display similar zonation as garnets from the Munsiari Formation (Figure 3). Fe concentration increases slightly from core (Xalm = 0.56) to rim (Xalm = 0.77), Ca content is constant from core to near the rim (Xgrs = 0.16) with a slight decrease at the rim (Xgrs = 0.11), Mg content is relatively homogeneous in the core (Xpyr = 0.02 average) with a slight enrichment at the rim (Xpyr = 0.1), and Mn content decreases from core (Xsps = 0.24) to near the rim (Xsps = 0.01) with a outer rim of enriched Mn. As in the Munsiari Formation, garnets in the the Joshimath Formation preserve growth zoning and do not show any evidence of modification by diffusion (i.e., flat Mn profile) (Figure 3). Garnets are nearly all euhedral except for minor rim resorption due to retrograde exchange reactions.

4.3. Pandukeshwar Formation (Middle GHS)

[20] Garnet porphyroblasts in the Pandukeshwar Formation have inclusion trails oriented nearly perpendicular to the external foliation (Figure 2c). These textures indicate ~90° (±30°) of rotation top-to-the-southwest. In the Pandukeshwar Formation, garnets are primarily poikiloblastic sieve garnets with bell-shaped growth zoning patterns at the base of the formation that grade to an increasingly homogenous composition at the top of the formation. Sample GH22–3 near the base of the formation has a decrease in Mn content from the core (Xsps = 0.07) to rim (Xsps = 0.02), while Fe, Mg, and Ca content remains constant from rim to core (Xalm = 0.87, Xpyp = 0.08, Xgrs = 0.01).

4.4. Badrinath Formation (Upper GHS)

[21] Garnet porphyroblasts in the Badrinath Formation are petrographically similar to those in the Joshimath Formation. However, calc-silicate layers within the Badrinath Formation commonly have groovy "atoll" garnets (Figure 2e). These garnets have commonly been interpreted as having two stages of growth wherein the core is compositionally distinct from the rim. Fractures in the garnet later allowed retrograde reactions to preferentially resorb the inner portion of the garnet leaving the unreacted rim preserved [*Smellie*, 1974; *Homam*, 2006]. These garnets are commonly cored with calcite and chlorite after biotite and muscovite. Muscovite in the middle portion of the formation has a symplectitic texture intergrown with chlorite and sericite, which indicates breakdown of muscovite due to increasing migmatization upsection [*Sachan et al.*, 2010]. The leucosomes associated with in situ muscovite dehydration consist of quartz + K-feldspar + plagioclase + muscovite ± biotite ± garnet ± tourmaline. In the restite, primary muscovite is absent and includes 2 cm diameter blebs of sillimanite expressed as fibrolite are present. The muscovite breakdown reaction,

$$\text{Muscovite} + \text{Quarts} + \text{Albite} = \text{K-feldspar} + \text{Sillimanite}/\text{Kyanite} + \text{Liquid}$$

best explains the mineralogy and textures of the Badrinath Formation as recognized elsewhere in the upper GHS units of the Himalayan orogen [e.g., *Inger and Harris*, 1992; *Harris and Massey*, 1994; *Davidson et al.*, 1997; *Daniel et al.*, 2003; *Kohn*, 2008].

[22] Garnets from the Badrinath Formation are found only within migmatitic gneiss. Compositional maps of representative garnets show that they are nearly homogeneous with respect to major cations, except for the outer ~10μm rim in which there is a significant increase in Mn (Figure 3). There is also a slightly more gradual increase in Fe content from the core (Xalm = 0.65) to rim (Xalm = 0.74) and decrease in Mg from the core (Xpyr = 0.26) to rim (Xpyr = 0.18). Due to lack of Mn-bearing phases in the matrix the increase in Mn is attributed to resorption of the garnet.

5. Geothermobarometry

[23] Pressure-temperature conditions (Table 1 and Figure 4) were calculated from standard mineral equilibria and the program GeoThermoBarometry (GTB) [*Spear et al.*,

[1] Auxiliary materials are available in the HTML. doi:10.1029/2010TC002853.

Table 1. Thermobarometric Results From Rocks of the Eastern Garhwal Region of India

Sample	MCT[a] (km)	T[b] (°C)	P (kbar)	Mineral[c]	T/d	Depth	Formation
GH4b	−2.0	550 ± 25	5.1 ± 0.5	Gt-Pl-Ms-Bt	30.2	18.2	*Munsiari*
		560 ± 30		Ti in Bt			
GH39b	−0.3	565 ± 25	8.8	Gt-Pl-Ms-Bt	18.0	31.4	*Munsiari*
GH14	−0.2	575 ± 25	8.2 ± 0.2	Gt-Pl-Al-Qtz	19.6	29.3	*Munsiari*
		560 ± 50		Ti in Bt			
GH15	0.1	580 ± 30	11.7 ± 0.8	Gt-Pl-Al-Qtz	13.9	41.8	*Munsiari*
		590 ± 60		Ti in Bt			
57A21	0.9	760 ± 25	14.1	Gt-Pl-Al-Qtz	15.1	50.4	Joshimath
GH41	1.0	690 ± 25	12.9 ± 0.2	Bt-Tm,Gt-Pl-Al-Qtz	15.0	46.1	Joshimath
GH16	1.1	725 ± 10	13.1 ± 0.5	Gt-Pl-Ms-Bt	15.5	46.8	Joshimath
		735 + 20		Bt-Tm			
GH17	1.4	740 ± 25	10 ± 0.1	Gt-Pl-Ms-Bt	20.7	35.7	Joshimath
60A	2.6	835 ± 25	14.9	Gt-Pl-Ms-Bt	15.7	53.2	Joshimath
GH18	2.8	790 ± 20					Joshimath
GH20	3.1	795 ± 20					Joshimath
GH43	4.2	720 ± 25	13 ± 0.3	Gt-Pl-Al-Qtz	15.5	46.4	Joshimath
GH21	4.9	760 ± 25	13.7 ± 0.8	Gt-Pl-Ms-Bt	15.5	48.9	Joshimath
GH25	7.2	810 ± 25	14.2 ± 0.2	Gt-Pl-Al-Qtz	16.0	50.7	Pandukeshwar
		785 ± 25		Bt-Tm			
GH48	11.7	860 ± 30	14.1 ± 0.7	Gt-Pl-Ms-Bt	17.1	50.4	Pandukeshwar
GH33b	15.1	810 ± 35					Badrinath
GH32b	15.1	825 ± 5		Bt-Tm			Badrinath
10A	19.6	810 ± 25	10.6	Gt-Pl-Ms-Bt	21.4	37.9	Badrinath
GH51b	20.1	810 ± 25	9.7 ± 0.6	Gt-Pl-Al-Qtz	23.5	34.6	Badrinath
GH54	22.1	860 ± 25	8.5 ± 0.1	Gt-Pl-Al-Qtz	28.3	30.4	Badrinath

[a]Stratigraphic distance above MCT. Assuming 45° dip.
[b]Rounded to nearest 5°C.
[c]Ti in Bt [*Henry et al.*, 2005], Bt-Tm [*Colopietro and Friberg*, 1987], Gt-Pl-Ms-Bt [*Hoisch*, 1990], Gt-Pl-Al-Qtz (*Koziol* [1989] with *Berman* [1990] Gt model).

1991; F. S. Spear and M. J. Kohn, Program GTB: GeoThermoBarometry, unpublished software, 2001, available at http://ees2.geo.rpi.edu/MetaPetaRen/Software/GTB_Prog/GTB.html] using garnet-biotite Fe-Mg exchange and biotite-tourmaline Fe-Mg exchange thermometers (*Ferry and Spear* [1978] with the *Berman* [1990] garnet activity model; *Colopietro and Friberg* [1987]), as well as the garnet-plagioclase-muscovite-biotite and garnet-plagioclase-aluminosilicate-quartz (*Hoisch* [1990] and *Koziol and Newton* [1988] with *Berman* [1990] garnet activity model) barometers. The Ti content in biotite has been shown to increase as a function of temperature [*Henry et al.*, 2005] and provides reliable temperatures from 480 to 800°C. *Kohn* [2008] found the use of THERMOCALC [*Powell and Holland*, 1988, 1994; *Holland and Powell*, 1998] yields results within error of these thermobarometric calculations. Analytical uncertainties are typically ±5°C and 0.25–0.5 kbar [*Kohn and Spear*, 1991]. However, the geological uncertainty with choosing the most appropriate mineral compositions far outweigh any analytical imprecision [*Daniel et al.*, 2003].

[24] Rim compositions were used for thermobarometry in garnets with no evidence of retrograde net-transfer or exchange reactions. Garnet compositions with the lowest Fe/(Fe + Mg) and Mn (that is near rim) were used as a close approximation of the garnet composition prior to resorption and diffusion effects during the highest grade metamorphic event, because these probably correspond most closely to the composition present at the peak temperature [*Spear*, 1993; *Kohn*, 2003]. For samples showing retrograde-exchange reactions, corrections are made to adjust for the Fe/Mg ratio in matrix biotite following the method of *Kohn and Spear* [2000]. Matrix biotite compositions are analyzed as line transects across biotite clusters and are chemically homogeneous in each sample. An average of the matrix biotite composition was used for geothermometric calculations. Muscovite analyses were conducted as line transects across several sheaths in the matrix of the samples. Both biotite and muscovite grains were analyzed at variable distances from garnet and show minimal zoning that varies with distance from garnet and therefore an average of the muscovite analyses was used. To estimate metamorphic pressures at the peak temperatures the rim composition of plagioclase was used. Compositional transects across tourmaline revealed strong zoning so rim compositions were used to estimate compositions that were in equilibrium with matrix biotite. Despite the tourmaline-biotite thermometer having only been calibrated for temperatures <600°C [*Abu El-Enen and Okrusch*, 2007], the higher temperatures we obtained (~830°C) are consistent with garnet-biotite thermometry from nearby samples.

[25] Phase equilibrium constraints [*Kohn*, 2008] were also considered in estimating temperatures and corresponding pressures (see Figure 7). The muscovite dehydration melting reaction occurs at a minimum temperature of ~700°C [*Spear et al.*, 1999] and the presence of kyanite-bearing migmatites in the Badrinath Formation implies minimum pressures of 8 kbar [*Davidson et al.*, 1997; *Spear et al.*, 1999; *Daniel et al.*, 2003; *Kohn*, 2008]. For pressures >8 kbar, the staurolite-in and kyanite-in reactions occur at minimum temperatures of ~575 and ~600°C, respectively [*Spear and Cheney*, 1989]. For temperatures <500°C, the presence of kyanite in the Joshimath Formation implies minimum pressures of ~3.8 kbar [*Spear et al.*, 1999]. Mg-rich cordierite-bearing migmatites in the Badrinath

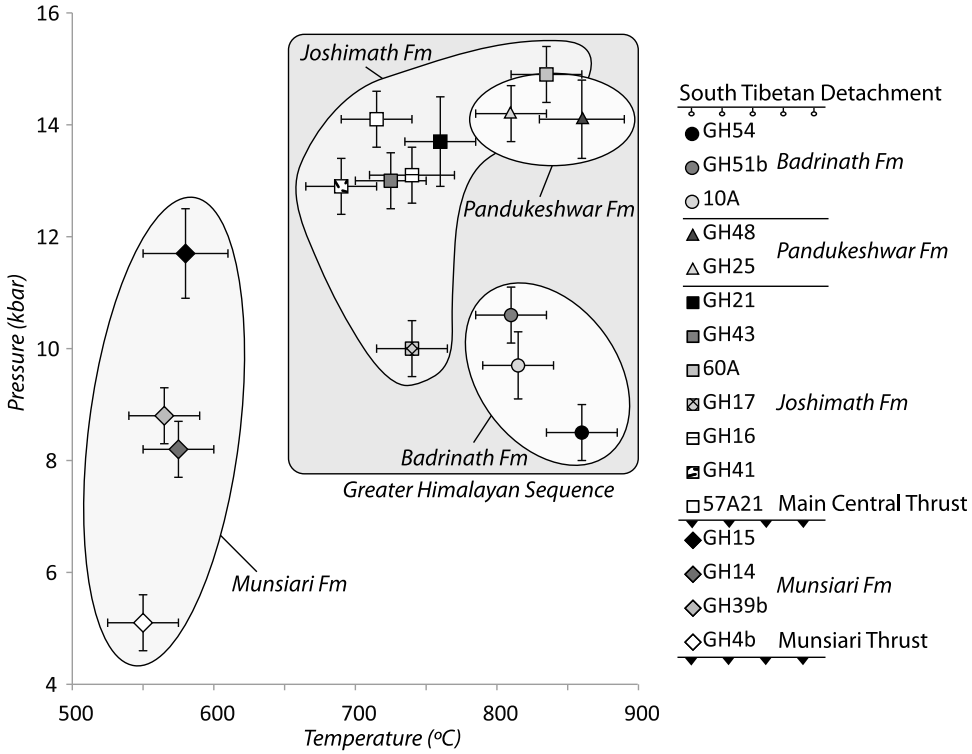

Figure 4. Inferred average pressure-temperature condition for samples from the Munsiari Formation and Greater Himalayan Sequence. Pressure-temperature conditions (Table 1) were calculated from standard mineral equilibria and program GeoThermoBarometry (GTB) [*Spear et al.*, 1991; Spear and Kohn, unpublished software, 2001].

Formation with calculated pressures between 7 and 10 kbar imply minimum temperatures of ~825–850°C [*Spear et al.*, 1999].

[26] The P-T estimates of the Munsiari Formation display a steep inverted pressure gradient at peak temperature of 2 kbar/km with pressures of ~5 kbar near the Munsiari Thrust and ~11.5 kbar toward the MCT (Figure 7). Temperatures are constant within error at 550–575°C. Continuing up section, P-T estimates remain roughly constant through the Joshimath and Pandukeshwar Formations with pressures ranging between 13 and 15 kbar and average temperatures of 785°C. Within the Badrinath Formation, temperatures range from 810 to 860°C; however pressures drop to from ~15 kbar to 8.5 kbar upsection to the STD.

6. Temperatures of Recrystallization

[27] *Stipp et al.* [2002] quantified three mechanisms of dynamic recrystallization of quartz are bulging (~280–400°C), subgrain rotation (~400–500°C), and grain boundary migration (~500°C and above). Chessboard extinction and amoeboid grain boundaries form at even higher temperatures. Chessboard extinction has been interpreted to represent basal and prismatic subgrain slip [*Mainprice et al.*, 1986; *Blumenfeld et al.*, 1986], and is estimated to occur at minimum temperatures of ~630°C [*Stipp et al.*, 2002; *Mancktelow and Pennacchioni*, 2004]. Due to the pressure dependence of this recrystallization mechanism [*Kruhl*, 1996], the temperature at which this texture is present increases to above ~800°C at 10 kbar [*Passchier and Trouw*, 2005]. Recrystallization of K-feldspar into subgrains is also observed throughout the entire GHS, which requires minimum temperatures of ~450°C [*Simpson and Wintsch*, 1989].

[28] Using these microstructures as a proxy for minimum recrystallization temperature provides temperature estimates independent from mineral chemistry and conventional thermobarometry, assuming that the last recrystallization recorded in the rock occurred at the same time as the peak temperature of metamorphism (Figures 5 and 7). However, within 0.5 km of the MCT there is an obvious temperature discontinuity reflected in the textural change in quartz microstructure to chessboard and amoeboid features dependent on temperatures in excess of >650°C.

[29] At this point the microtexture changes to the higher temperature form of chessboard and amoeboid features (>650°C). These features persist throughout the entire GHS. Little to no quartz dynamic recrystallization is found in the Martoli Formation above with only minor grain boundary bulging closest to the STD. Although it is unclear to what degree these quartz recrystallization fabrics have been retrogressed it is clear the thermal pattern is closely matched to that of the thermobarometry.

7. Phases of Deformation

[30] Two deformational phases are recognizable within the Munsiari Formation and the GHS. The earlier phase is associated with the formation of a regional penetrative foliation (S1), that is parallel to S0 and to the Munsiari and

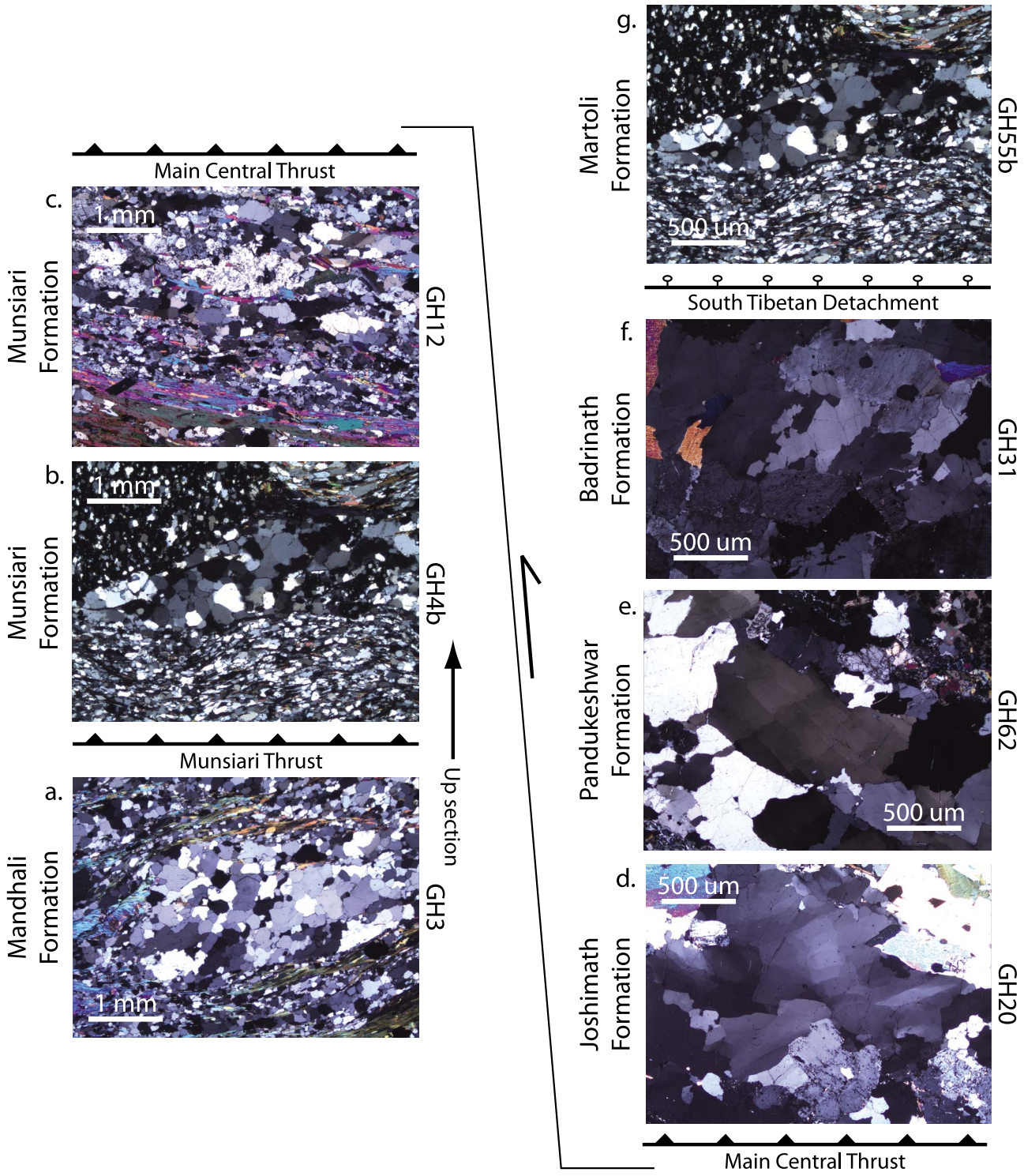

Figure 5. Photomicrographs (cross-polarized light) illustrating quartz recrystallization microstructures. Refer to Figures 1 and 2. All thin sections are cut perpendicular to S1, and parallel to identifiable mineral stretching lineation. Quartz microstructure classification and temperature estimates defined by *Stipp et al.* [2002]. Thin sections are in tectonostratigraphic order from lowest (Figures 5a–5c) to highest (Figures 5d–5g): (a) Mandhali Formation quartzite and quartz-rich schist, (b, c) Munsiari Formation garnet schist exhibiting bulging recrystallization (>300°C), (d, e) kyanite gneiss and quartzofelspathic gneiss exhibiting chessboard extinction (≥630°C), (f) migmatitic gneiss with classic amoeboid grain boundary migration with chessboard extinction (≥630°C), and (g) slate with quartz viens with minor bulging recrystallization (>300°C).

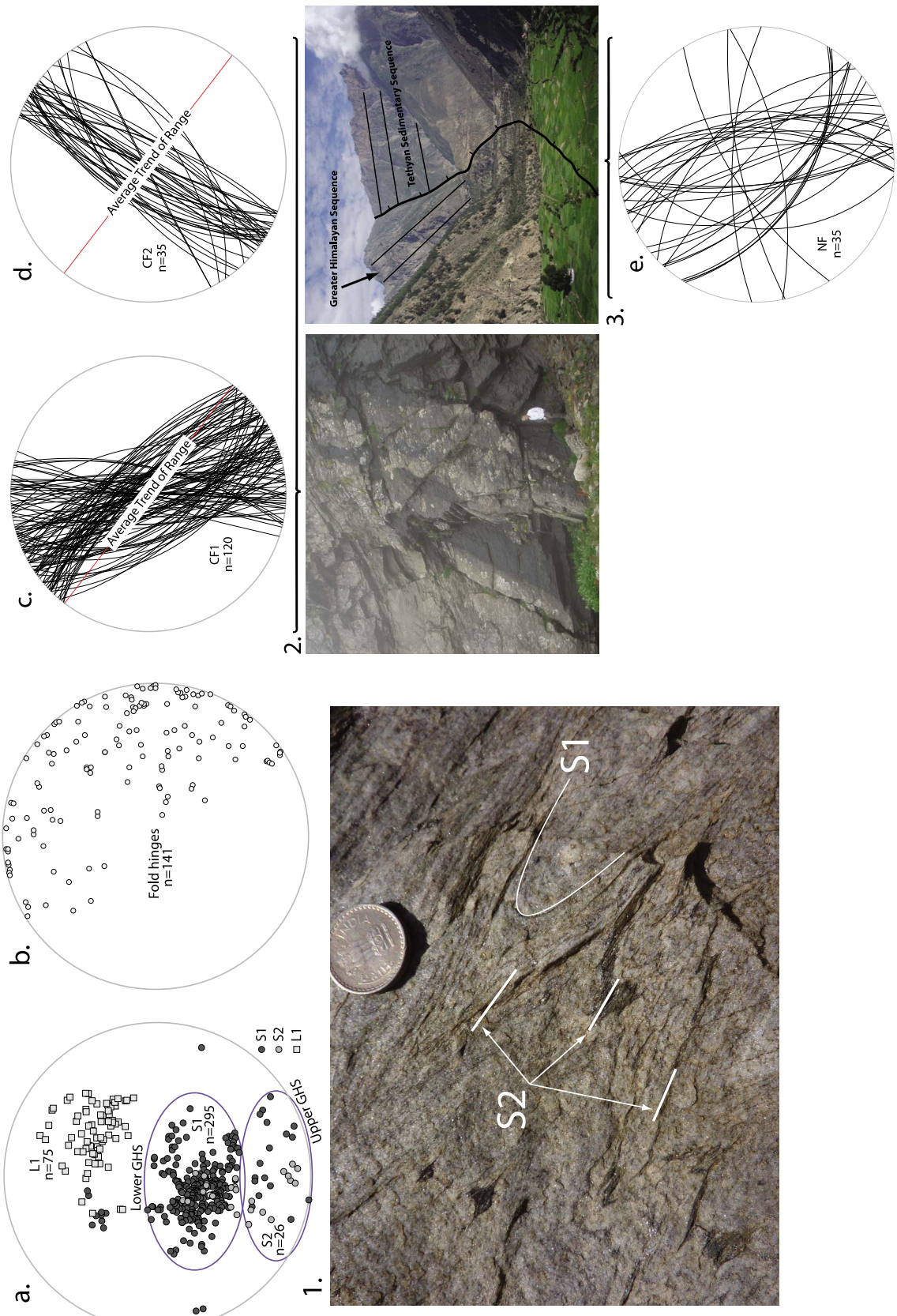

Figure 6. Ductile and brittle structure of the Greater Himalayan Sequence. Stereographs are equal-area, lower-hemisphere projections: (a) mineral stretching lineations (L1) and poles to the dominant penetrative foliation (S1) and axial planar foliation (S2); (b) fold hingelines; (c) orogen-parallel conjugate fracture plans (d) orogen perpendicular conjugate fracture planes, and (e) normal fault planes, South Tibetan Detachment (STD). Photographs of (1) folded S1 foliation and axial planar S2 foliation,(2) conjugate fractures in the Rishiganga near Badrinath, and (3) the South Tibetan Detachment at Malari looking northwest.

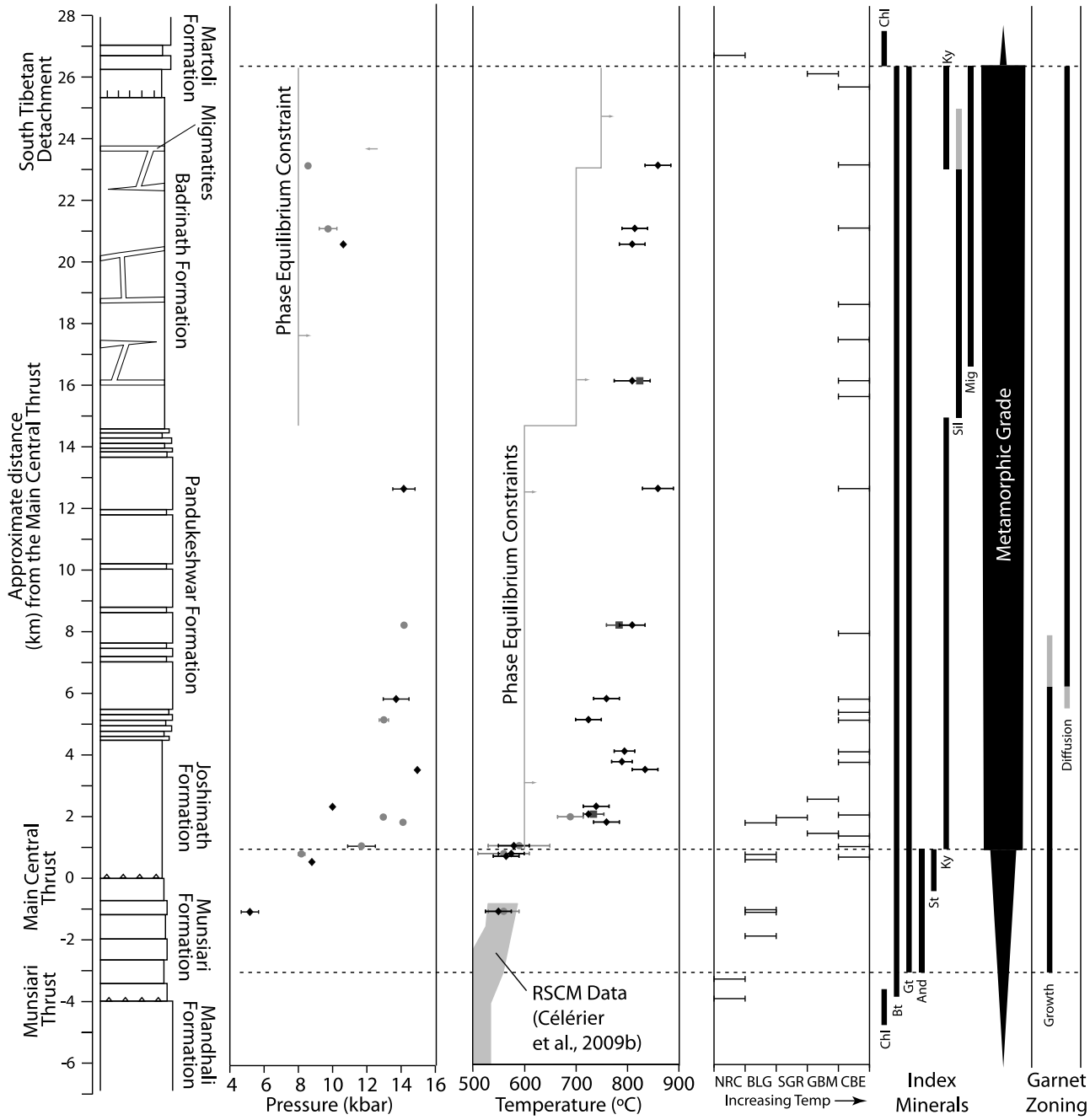

Figure 7. Tectonostratigraphic column with stratigraphic locations of pressure and temperature estimates, temeratures estimates from quartz recystalization fabrics [after *Stipp et al.*, 2002], metamorphic index minerals, and representative garnet zoning. Due to the near homoclinal nature of the Greater Himalayan Sequence, P-T conditions are plotted versus structural distance with respect to the Main Central Thrust, assuming a constant dip angle of 45° [*Macfarlane et al.*, 1992; *Kohn*, 2008]. In the pressure field diamonds represent Gt-Pl-Ms-Bt barometry [*Hoisch*, 1990] and circles represent Gt-Pl-AlSiO5-Qtz barometry (*Koziol and Newton* [1989] with the *Berman* [1990] garnet activity model). Phase equilibria constraints are from *Kohn* [2008]. In the temperature field circles represent the Ti in Bt thermometry [*Henry et al.*, 2005], diamonds represent the Gt-Bt thermometry (*Ferry and Spear* [1978] with the *Berman* [1990] garnet activity model), and squares represent the Bt-Tm thermometry [*Colopietro and Friberg*, 1987]. Raman Spectroscopy of Carbonaceous Material (RSCM) thermometry from *Célérier et al.* [2009b]. Quartz recrystallization fabrics abbreveations are NRC: no recrystallization; BLG: bulging grain boundaries; SGR: sub-grain rotation; GBM: grain boundary migration; CBE: chessboard extinction. Garnet zoning patterns primarily defined by Mn zoning. Compare with *Goscombe et al.* [2006] and *Jessup et al.* [2008].

MCTs (Figure 6a). S0 is defined as the original sedimentary layering and is not readily indentifable. S1 is associated mostly with general shear as indicated by S-C fabrics found throughout the GHS with high degrees of non-coaxial shear in the more pelitic units. For example, the angle between the S and C planes decreases from ∼30° in the middle of the GHS to ∼15–20° in proximity to the MCT. In these shear fabrics, S is equal to S1 and C is equal to S2 (see below).

[31] A second foliation (S2) is locally developed; it is found throughout the GHS and is mostly parallel to axial surfaces of small scale isoclinal folds of S1 (Figure 6a). These two fabrics most likely developed under the same progressive ductile flow regime.

[32] Tight isoclinal and recumbent folds are found localized at the MCT and in weak pelite-rich zones throughout the GHS. All of the folds show top to the SW fold-asymmetry with the exception of those found near the STD which are top to the NE. The opposite vergence of folds at the base and top of the GHS is consistent with ductile flow between the MCT and STD. It is unclear whether ductile flow with opposite sense was coeval or sequential as no fold interference features were observed.

[33] Fold hinges within the GHS from the Eastern Garhwal region of India display nearly 150° variation from NW to SSE (Figure 6b). These data are consistent with a single "flow" event accommodated by sheath folds. Mineral stretching lineations plunge to the northeast, which is consistent with sheath fold flow direction. Recognizable sheath folds in outcrop within the GHS of the Garhwal region range in scale from several centimeters to several meters. However, the extent of variation in hinge azimuth predicts that an even larger scale sheath folds exist that exceed the size of the outcrops available.

[34] Ductile flow was accommodated in many places throughout the Munsiari Formation and the GHS by sheaths folds. In addition to the ductile shortening features described above, late stage orogen parallel and perpendicular extension features are recognized throughout the GHS through the entire orogen [*Janda et al.*, 2002; *Vannay et al.*, 2004; *Thiede et al.*, 2004; *Jessup et al.*, 2008; *Hintersberger et al.*, 2010]. In the Eastern Garhwal region, these normal faults and associated conjugate shear fractures (Figures 6c and 6d) crosscut the major tectonic boundaries of the GHS and are found throughout the LHCS and the lower portion of the TSS.

7.1. Extension Perpendicular to the Orogen

[35] Near the town of Malari, the STD consists of a 1–2 km wide ductile shear zone with top-down-to-the-NE folds and is overprinted by a discrete brittle fracture zone 10–30 m thick that dips to the north ∼35–45°. It was previously reported [*Gururajan and Choudhuri*, 1999; *Sachan et al.*, 2010] that the normal fault associated with the uppermost portion of the STD is crosscut by the Malari Leucogranite. However, despite granitic material found in the damage zone of the fault, we found no granite intruding the Tethyan Sequence and that the low-angle normal fault cuts around the main body of the intrusion in a similar way to low-angle faults forming turtle-back structures in Western North America (i.e., Death Valley) [*Çemen et al.*, 2005].

[36] Normal faults and conjugate fractures oriented parallel to the orogen found throughout the GHS have an average strike of 337° (Figure 6c), which is similar to the average trend of the range in this area (310°). These brittle structures increase in frequency upsection toward the STD. Most orogen parallel normal faults we measured have minor displacements (<10 m) with mostly top down to the ENE. These faults strike subparallel to the Southern Tibetan Detachment (Figures 6c and 6d). Similar extensional features, such as the Karcham Normal Fault Zone, are reported along the Sutlej transect [*Janda et al.*, 2002; *Vannay et al.*, 2004; *Thiede et al.*, 2004; *Hintersberger et al.*, 2010].

7.2. Extension Parallel to the Orogen

[37] Conjugate fractures and normal faults oriented perpendicular to the range with an average trend of 037° (Figure 6d) are less prevalent than those oriented parallel to the range. They are also found throughout the entire Himalayan Range. Major orogen parallel extension south of the STD is also documented elsewhere in the range [*Meyer et al.*, 2006; *Jessup et al.*, 2008; *Hintersberger et al.*, 2010; *Kali et al.*, 2010; *Langille et al.*, 2010]. How orogen parallel extension relates temporally and kinematically with the orogen perpendicular extension is unclear, but both could be associated with the same late-stage phase of extensional exhumation, if the intermediate and minimum stresses were nearly the same and sub-horizontal.

[38] Applying a similar relationship described in the Marsyandi area of central Nepal, *Coleman* [1996] describes a change from orogen-perpendicular extension in the orogenic core early in deformational history superimposed by orogen parallel extension later in the deformation. However, this relationship is described within discrete fault zones associated with the STD (as opposed to a wide zone with an indeterminable amount of extension) and is not represented as a regional phenomenon.

8. Discussion

[39] Combining the thermobarometry of the Munsiari Formation and the GHS with the thermometry of the LHCS of *Célérier et al.* [2009b] along the Alaknanda and Dhauliganga allows further characterization of the peak metamorphic temperatures from the Main Boundary Thrust to the STD (Figure 1). *Célérier et al.* [2009b] used Raman spectroscopy of carbonaceous material to obtain peak metamorphic temperatures in the LHCS from >330°C to ∼580°C, with temperatures increasing upsection to the Munsiari thrust (Figure 7). Garnet-biotite thermometry (this paper) show a slight upsection increase in temperatures from ∼550°C to 600°C nearest to the MCT. This slight increase in temperature could have been caused by an inversion of the isotherms due to the overthrusting of the hotter GHS on top of the colder LHCS. This results in significant retrograde exchange reactions and the resorption of garnets in the lowermost GHS. This is similar to the hot-iron-model proposed by *Le Fort* [1975], which predicts that, as a consequence of a retrograde metamorphic evolution in the hanging wall of the MCT, the temperature should increase upwards across the thrust zone. This is consistent with the slight upsection increase in temperature along the base of the GHS within two kilometers of the MCT. The PT profile

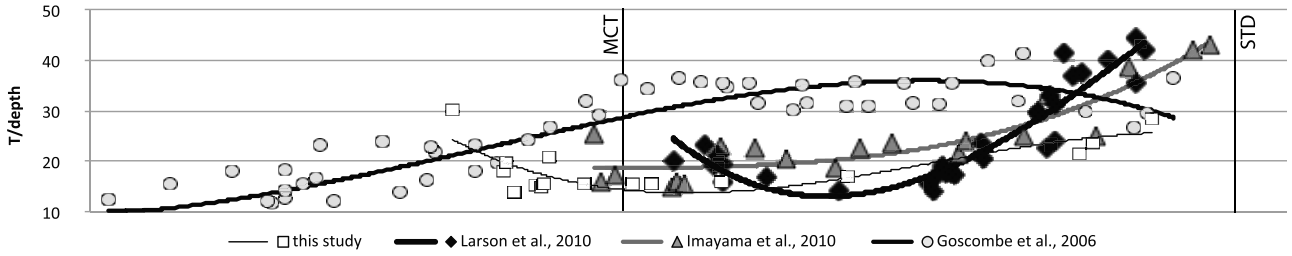

Figure 8. Comparison of temperature/depth ratios (T/depth) from Eastern Nepal [*Goscombe et al.*, 2006; *Imayama et al.*, 2010], Central Nepal [*Larson et al.*, 2010], and the Garhwal Region (this study). Despite the nonlinear nature of various parameters (e.g., uncertainties of rock densities and nonlinear nature of geotherms) uncertainties are assumed to effect all samples with a similar order of magnitude (assuming 2.8 g/cm3 density of an average metapelite). Taking these assumptions into account, the absolute values of the geothermal gradients may be questionable. However, because the assumptions are consistent in all samples, the relative difference between them is indisputable and can be used to infer the T/depth of the studied transects [see *Groppo et al.*, 2009]. The x axis represents normalized distance between MCT and STD. MCT, Main Central Thrust; STD, South Tibetan Detachment.

in the Garhwal region is similar to those found in Central Nepal [*Kohn*, 2008] and Eastern Nepal [*Imayama et al.*, 2010].

[40] The upper portion of the GHS in the Garhwal region contains increasing concentrations of migmatite and leucogranite. Isotope geochemistry of these leucogranites is indicative of a metasedimentary source most akin to the GHS [*Guillot and Le Fort*, 1995; *Searle*, 1999; *Ahmad et al.*, 2000]. Decompression during exhumation along the STD may have triggered partial melting of the crust, creating leucogranite bodies that rose into the uppermost levels of the GHS [*Searle*, 1999; *Harrison et al.*, 1998]. Whether these partial melts represent in situ melting or melt migration from a structurally lower portion of the crust is unresolved [*Harris*, 2007]. However, we confirmed some degree of in situ melting by documenting sillimanite-rich restites in the Badrinath Formation. The relatively evolved bulk chemical composition, high Rb/Sr ratio, and normative corundum of the Malari leucogranite indicate melting of a sedimentary source, likely the GHS [*Sachan et al.*, 2010]. The advection of heat associated with emplacement of leucogranites in the upper GHS (Badrinath Formation) can explain the elevated metamorphic temperatures we observe which is consistent with leucogranites found throughout the range [*Vidal et al.*, 1982; *Inger and Harris*, 1993; *Guillot and Le Fort*, 1995; *Searle et al.*, 1997; *Searle*, 1999; *Searle and Godin*, 2003; *Singh et al.*, 2003; *Nabelek and Liu*, 2004]. Compositional transects across representative garnets from each of the garnet-bearing formations show increasingly flat profiles (Ca, Mn, Mg, Fe) upsection in the Badrinath Formation (Figure 3). This pattern is attributed to the increased duration of time at which the Badrinath Formation was at peak temperature [*Caddick et al.*, 2010].

[41] Maximum calculated pressures at peak temperature in the Badrinath Formation decrease from ~14 kbar to 8.5 kbar near the STD at a rate of 710 bar/km (assuming average density of ~2800 km/m3). This apparent pressure gradient is nearly three times as high than expected from lithostatic pressure (270 bar/km) [*Hodges and Silverberg*, 1988; *Larson et al.*, 2010]. *Fraser et al.* [2000] reported a pressure gradient of 540 bar/km in the Langtang region of Central Nepal and *Larson et al.* [2010] reported a pressure gradient of ~620 bar/km in the Manaslu–Himal Chuli region of Central Nepal. However, it must be noted that peak metamorphic temperatures were achieved during isothermal decompression; therefore, the pressures at peak metamorphic temperatures may not be representative of peak metamorphic pressures. As mentioned by *Larson et al.* [2010], this high pressure gradient most likely results from post-metamorphic tectonic thinning of the crust. This interpretation is consistent with the brittle layer parallel extensional features we find throughout the GHS (e.g., vertical conjugate fractures and normal faults). However, it is difficult for us to account for significant layer-parallel extension unless a major component of the thinning of the GHS involved top-down-to-the-north extension via the STD or by flattening during top-up-to-the-south thrusting via the MCT, or a combination of the two via coeval motion along these bounding shear zones [*Larson et al.*, 2010]. North-verging fold-asymmetry in the upper GHS attests to some degree of top down to the SE ductile shear and layer parallel extension in the hanging wall of the STD. This is similar to what is seen in the Annapurna range [*Kellett and Godin*, 2009; *Searle*, 2010] and the tectonic thinning of the GHS is also predicted by numerical models of channel flow [*Beaumont et al.*, 2004; *Jamieson et al.*, 2004].

[42] Variations in thermobarometric patterns along orogenic strike in the GHS are used to better understand the relationship between the thermal history and spatial variations in erosion and exhumation rates of the Himalayan

Figure 9. Schematic diagrams of PT profiles predicted by channel flow models HT1 [*Jamieson et al.*, 2004] and HT111 [*Jamieson et al.*, 2006] and the observed PT profile from the Eastern Garhwal region. RSCM from the Alaknanda transect in the Eastern Garhwal region from *Célérier et al.* [2009a]. Note: stratigraphic distance from the Main Central Thrust only applies to the PT profile from the Eastern Garhwal region. MCT, Main Central Thrust; MT, Munsiari Thrust; STD, South Tibetan Detachment. Gt-Bt (garnet-biotite), Tr-Bt (tourmaline-biotite), Ti Bt (titanium in biotite) thermometry methods described in text.

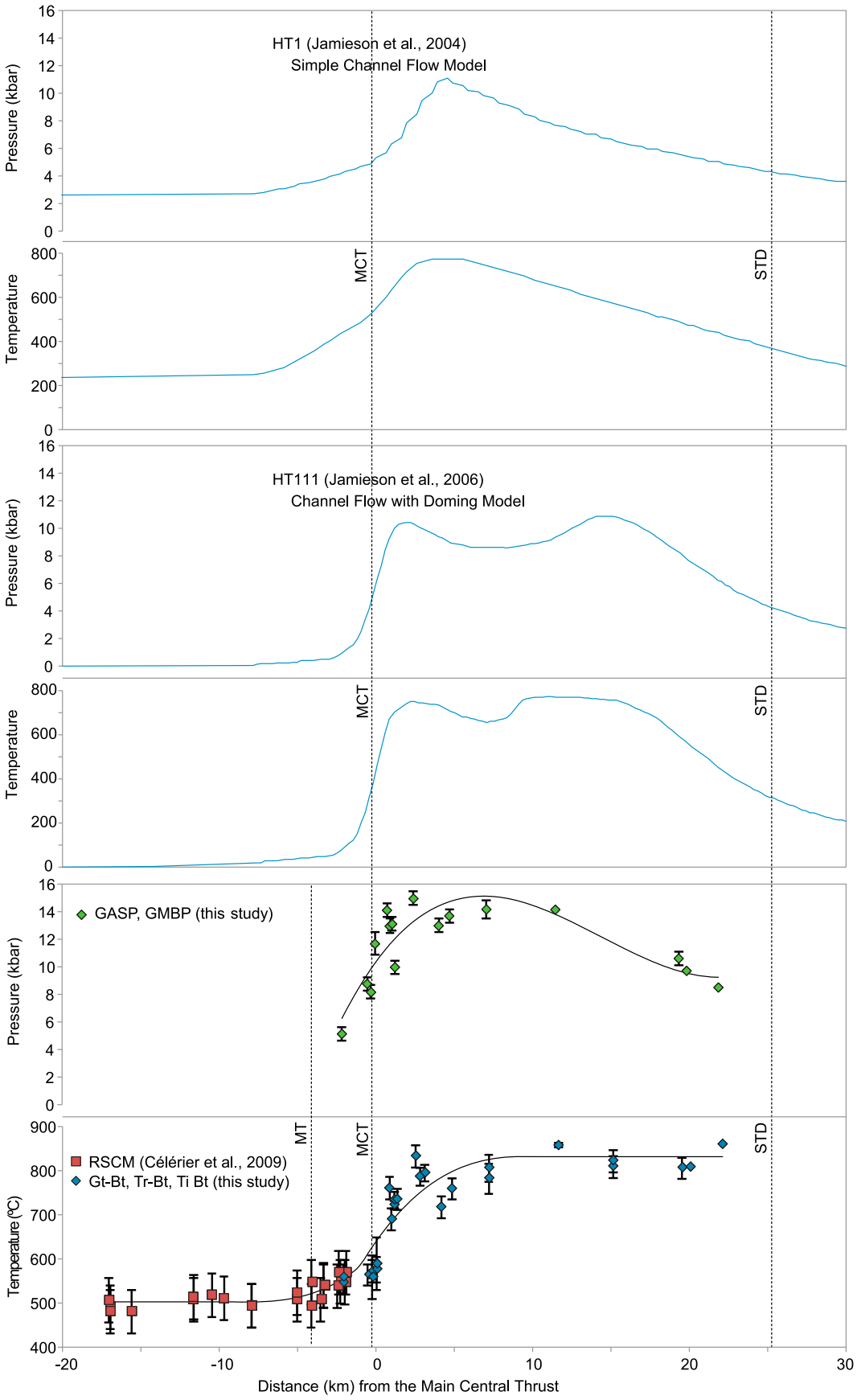
HT1 (Jamieson et al., 2004)
Simple Channel Flow Model
Pressure (kbar)
Temperature
MCT
STD
HT111 (Jamieson et al., 2006)
Channel Flow with Doming Model
GASP, GMBP (this study)
RSCM (Célérier et al., 2009)
Gt-Bt, Tr-Bt, Ti Bt (this study)
MT
Temperature (ºC)
Distance (km) from the Main Central Thrust

Figure 9

Orogen [*Spear et al.*, 1984; *Inger and Harris*, 1992; *Spear*, 1993; *Macfarlane*, 1995; *Jamieson et al.*, 1996; *Vannay and Hodges*, 1996; *Vannay et al.*, 1999; *Fraser et al.*, 2000; *Catlos et al.*, 2001; *Vannay and Grasemann*, 2001; *Daniel et al.*, 2003; *Goscombe et al.*, 2005, 2006; *Kohn*, 2008; *Imayama et al.*, 2010]. These spatial variations are plausible because the thermal evolution of orogenic belts is governed to a large extent by the competition between heat conduction and advection as material is transported through the crust at varying rates, which is influenced by erosion [*Goscombe et al.*, 2005]. Variation in the metamorphic gradient throughout the range is possibly due to variation in domain-specific parameters within the orogen, such as lithology, stages of magmatism, arrangement of shear zones, and erosion rates; all of which influence heat and material advection through the crust [*Beaumont et al.*, 2004; *Jamieson et al.*, 2004].

[43] The Eastern Garhwal region (Figure 7) has higher temperatures (700–850°C), higher pressures (12–15 kbar) and generally lower T/depth ratios (14–30°C/km) than those observed elsewhere in the range (Figure 8). The T/depth ratio pattern (Figure 7) shows a decrease upsection from the MCT, which is consistent with conductive heating of footwall rocks (the LHCS) and cooling of the hanging wall rocks (the GHS). At the top of the GHS, the T/depth ratio increases (Figure 7), consistent with conductive cooling of the GHS due to exhumation beneath the Southern Tibetan Detachment. This is similar to T/depth ratios documented in Central and Eastern Nepal [*Larson et al.*, 2010; *Imayama et al.*, 2010] (Figure 8).

[44] Numerical models of channel flow of *Jamieson et al.* [2004, 2006] (models HT1 and HT111) predict T/depth ratios for the GHS (18–27.5°C/km) (calculated by the authors of this study) that span a similar range as those found in the Eastern Garhwal region (14–30°C/km). The predicted pattern of the T/depth ratios predicted by the model HT1 also matches very closely to the pattern of Eastern Garhwal region.

[45] One important distinction between model predictions and field observations is the decreasing temperature with increasing structural level in the model HT1 of *Jamieson et al.* [2004] versus the observed nearly constant temperature throughout the GHS (Figure 7). The discrepancy may be ascribed to advective heat transfer by melt and fluid migration associated with migmatization and emplacement of the leucogranite bodies of the High Himalaya, which is not considered in the HT1 model. This process can potentially transfer large amounts of heat toward the structurally highest levels of the GHS [e.g., *Miyazaki*, 2007; *Depine et al.*, 2008; *Imayama et al.*, 2010]. In central Nepal, *Hodges and Silverberg* [1988] posit that widespread migmitization and melt-escape acted as a buffer to produce nearly uniform temperatures within the high-grade gneiss of the GHS. Adding this modification to the channel flow models (that is, addition of heat advection by melt and/or fluid migration) would lead to a lower predicted temperature gradient in the model, reflected in a low temperature gradient [*Imayama et al.*, 2010].

[46] The broad high temperature region at high structural level shown in the peak temperature profile (Figure 9) is however compatible with the dome extrusion style model (HT111) of *Jamieson et al.* [2006]. These models predict higher peak pressure at peak temperature over a broader region than HT1. Model HT111 is similar to HT1 except that the upper crust contains an embedded weak layer between 4.5 and 7 km depth made to represent weak sedimentary rock with high pore fluid pressure. This weak layer facilitates the detachment and outward flow of the upper crust overlying the channel. Consequently, the model channel propagates much farther to the south in HT111 than it does in HT1, forcing the foreland fold and thrust belt farther into the foreland basin.

9. Conclusion

[47] The metamorphic rocks of the High Himalayas in the Eastern Garhwal region of northwest India yield peak metamorphic conditions in the Munsiari Formation of 550–600°C and 5–9 kbar. Peak metamorphic conditions near the base of the structurally overlying GHS range from 700 to 800°C and 10–12 kbar, revealing a stark discontinuity between the GHS and LHCS. Peak metamorphic temperature, calculated from mineral equilibria remain nearly constant (~800–850°C) through the rest of the GHS to the STD. Peak temperature metamorphic pressures increase from 12 to 14 kbar 3 km above the the MCT, then decrease to 9 kbar at the South Tibetan Detachment. Quartz recrystallization temperatures also reveal a major metamorphic discontinuity between the LHCS and the GHS. A slight upturn in metamorphic temperatures in the footwall (LHCS) and downturn in the hanging wall (GHS) across the MCT is evidence for modification of the temperature profiles most likely due to a "hot iron effect" of thrusting the hotter GHS on top of the LHCS.

[48] The thermobarometric profiles found in the Garhwal Himalaya are generally consistent with the patterns predicted by numerical models of channel flow [*Beaumont et al.*, 2004; *Jamieson et al.*, 2006]. The extensional conjugate fractures found throughout the metamorphic core imply the most recent deformation occurred in a supercritical wedge.

[49] **Acknowledgments.** The authors thank Talat Ahmad, Himanshu Sachan, and Ashutosh Kainthola for help with field work and logistics. We are also grateful to Djordje Gruijic, Jen Chambers, and two anonymous reviewers for very helpful editorial comments that resulted in a much improved manuscript.

References

Abu El-Enen, M. M., and M. Okrusch (2007), The texture and composition of tourmaline in metasediments of the Sinai, Egypt. Implications for the tectono-metamorphic evolution of the Pan-African basement, *Mineral. Mag.*, *71*, 17–40, doi:10.1180/minmag.2007.071.1.17.

Ahmad, T., N. Harris, M. Bickle, H. Chapman, J. Bunbury, and C. Prince (2000), Isotopic constraints on the structural relationships between the Lesser Himalayan Series and the High Himalayan Crystalline Series, Eastern Garhwal Himalaya, *Geol. Soc. Am. Bull.*, *112*, 467–477, doi:10.1130/0016-7606(2000)112<467:ICOTSR>2.0.CO;2.

Beaumont, C., R. A. Jamieson, M. H. Nguyen, and B. Lee (2001), Himalayan tectonics explained by extrusion of a low-viscosity crustal channel coupled to focused surface denudation, *Nature*, *414*, 738–742, doi:10.1038/414738a.

Beaumont, C., R. A. Jamieson, M. H. Nguyen, and S. Medvedev (2004), Crustal channel-flows. 1, Numerical models with applications to the tectonics of the Himalayan-Tibetan orogen, *J. Geophys. Res.*, *109*, B06406, doi:10.1029/2003JB002809.

Beaumont, C., M. Nguyen, R. Jamieson, and S. Ellis (2006), Crustal flow modes in large hot orogens, in *Channel Flow, Ductile Extrusion and Exhumation in Continental Collision Zones*, edited by R. D. Law, M. P. Searle, and L. Godin, *Geol. Soc. Spec. Publ.*, *268*, 91–145.

Berman, R. G. (1990), Mixing properties of Ca-Mg-Fe-Mn garnets, *Am. Mineral.*, *75*, 328–344.

Blumenfeld, P., D. Mainprice, and J. L. Bouchez (1986), C-slip in quartz from subsolidus deformed granite, *Tectonophysics*, *27*, 271–294.

Burchfiel, B. C., Z. Chen, K. V. Hodges, Y. Liu, L. H. Royden, C. Deng, and J. Xu (1992), The South Tibetan Detachment System, Himalayan Orogen, *Spec. Pap. Geol. Soc. Am.*, *269*, 41 pp.

Caddick, M. J., J. Konopásek, and A. B. Thompson (2010), Preservation of garnet growth zoning and the duration of prograde metamorphism, *J. Petrol.*, *51*, 2327–2347, doi:10.1093/petrology/egq059.

Carosi, R., C. Montomoli, D. Rubatto, and D. Visona (2006), Normal-sense shear zones in the core of the Higher Himalayan Crystallines (Bhutan Himalaya): Evidence for extrusion?, in *Channel Flow, Ductile Extrusion and Exhumation in Continental Collision Zones*, edited by R. D. Law, M. P. Searle, and L. Godin, *Geol. Soc. Spec. Publ.*, *268*, 425–444.

Catlos, E. J., T. M. Harrison, M. J. Kohn, M. Grove, F. J. Ryerson, C. Manning, and B. N. Upreti (2001), Geochronologic and thermobarometric constraints on the evolution of the MCT, central Nepal Himalaya, *J. Geophys. Res.*, *106*, 16,177–16,204, doi:10.1029/2000JB900375.

Célérier, J., T. M. Harrison, A. A. G. Webb, and A. Yin (2009a), The Kumaun and Garwhal Lesser Himalaya, India. Part 1, Structure and stratigraphy, *Geol. Soc. Am. Bull.*, *121*, 1262–1280, doi:10.1130/B26344.1.

Célérier, J., T. M. Harrison, O. Beyssac, F. Herman, W. J. Dunlap, and A. A. G. Webb (2009b), The Kumaun and Garwhal Lesser Himalaya, India. Part 2, Thermal and deformation histories, *Geol. Soc. Am. Bull.*, *121*, 1281–1297, doi:10.1130/B26343.1.

Çemen, I., O. Tekeli, G. Seyitoglu, and V. Isik (2005), Are turtleback fault surfaces common structural elements of highly extended terranes?, *Earth Sci. Rev.*, *73*, 139–148, doi:10.1016/j.earscirev.2005.07.001.

Coleman, M. E. (1996), Orogen-parallel and orogen-perpendicular extension in the central Nepalese Himalayas, *Geol. Soc. Am. Bull.*, *108*, 1594–1607, doi:10.1130/0016-7606(1996)108<1594:OPAOPE>2.3.CO;2.

Colopietro, M. R., and L. M. Friberg (1987), Tourmaline-biotite as a potential geothermometer for metape-lites; Black Hills, South Dakota, *Geol. Soc. Am. Abstr. Programs*, *19*, 624.

Cottle, J. M., M. J. Jessup, D. L. Newell, M. P. Searle, R. D. Law, and M. S. A. Horstwood (2007), Structural insights into the early stages of exhumation along an orogen-scale detachment: The South Tibetan detachment system, Dzakaa Chu section, Eastern Himalaya, *J. Struct. Geol.*, *29*, 1781–1797, doi:10.1016/j.jsg.2007.08.007.

Daniel, C. G., L. S. Hollister, R. R. Parrish, and D. D. Grujic (2003), Exhumation of the MCT from lower crustal depths, eastern Bhutan Himalaya, *J. Metamorph. Geol.*, *21*, 317–334, doi:10.1046/j.1525-1314.2003.00445.x.

Davidson, C., D. E. Grujic, L. S. Hollister, and S. M. Schmid (1997), Metamorphic reactions related to decompression and synkinematic intrusion of leucogranite, High Himalayan Crystallines, Bhutan, *J. Metamorph. Geol.*, *15*, 593–612, doi:10.1111/j.1525-1314.1997.00044.x.

Depine, V. G., C. L. Andronicos, and J. P. Morgan (2008), Near-isothermal conditions in the middle and lower crust induced by melt migration, *Nature*, *452*, 80–83, doi:10.1038/nature06689.

Ferry, J. M., and F. S. Spear (1978), Experimental calibration of the partitioning of Fe and Mg between biotite and garnet, *Contrib. Mineral. Petrol.*, *66*, 113–117, doi:10.1007/BF00372150.

Fraser, G., B. Worley, and M. Sandiford (2000), High-precision geothermobarometry across the High Himalayan metamorphic sequence, Langtang Valley, Nepal, *J. Metamorph. Geol.*, *18*, 665–681, doi:10.1046/j.1525-1314.2000.00283.x.

Goscombe, B., D. Gray, and M. Hand (2005), Extrusional tectonics in the core of a transpressional orogen; the Kaoko Belt, Namibia, *J. Petrol.*, *46*, 1203–1241, doi:10.1093/petrology/egi014.

Goscombe, B., D. Gray, and M. Hand (2006), Crustal architecture of the Himalayan metamorphic front in eastern Nepal, *Gondwana Res.*, *10*, 232–255, doi:10.1016/j.gr.2006.05.003.

Groppo, C., F. Rolfo, and B. Lombardo (2009), P-T evolution across the MCT Zone (eastern Nepal): Hidden discontinuities revealed by perology, *J. Petrol.*, *50*, 1149–1180, doi:10.1093/petrology/egp036.

Guillot, S., and P. Le Fort (1995), Geochemical constraints on the bimodal origin of High Himalayan leucogranites, *Lithos*, *35*, 221–234, doi:10.1016/0024-4937(94)00052-4.

Gururajan, N. S., and B. K. Choudhuri (1999), Ductile thrusting, metamorphism and normal faulting in Dhauliganga Valley, Garhwal Himalaya, *Himal. Geol.*, *20*, 19–29.

Harris, N. (2007), Channel flow and the Himalayan-Tibetan orogen: A critical review, *J. Geol. Soc.*, *164*, 511–523, doi:10.1144/0016-76492006-133.

Harris, N., and J. Massey (1994), Decompression and anatexis of Himalayan metapelites, *Tectonics*, *13*, 1537–1546, doi:10.1029/94TC01611.

Harrison, T. M., M. Grove, O. M. Lovera, and E. J. Catlos (1998), A model for the origin of Himalayan anatexis and inverted metamorphism, *J. Geophys. Res.*, *103*, 27,017–27,032, doi:10.1029/98JB02468.

Henry, D. J., C. V. Guidotti, and J. A. Thomson (2005), The Ti-saturation surface for low-to-medium pressure metapelitic biotites. Implications for geothermometry and Ti-substitution mechanisms, *Am. Mineral.*, *90*, 316–328, doi:10.2138/am.2005.1498.

Hintersberger, E., R. C. Thiede, M. R. Strecker, and B. R. Hacker (2010), East-west extension in the NW Indian Himalaya, *Geol. Soc. Am. Bull.*, *122*, 1499–1515, doi:10.1130/B26589.1.

Hodges, K. V., and D. S. Silverberg (1988), Thermal Evolution of the Greater Himalaya, Garhwal, , India, *Tectonics*, *7*, 583–600, doi:10.1029/TC007i003p00583.

Hoisch, T. D. (1990), Empirical calibration of six geobarometers for the mineral assemblage quartz + muscovite + biotite + plagioclase + garnet, *Contrib. Mineral. Petrol.*, *104*, 225–234, doi:10.1007/BF00306445.

Holland, T. J. B., and R. Powell (1998), An internally consistent thermodynamic data set for phases of petrological interest, *J. Metamorph. Geol.*, *16*, 309–343, doi:10.1111/j.1525-1314.1998.00140.x.

Homam, S. M. (2006), The occurence and origin of atoll garnet in hornblende schist from the contact aureole of the Mashhad Granite, NE Iran, *Iran. J. Sci. Technol., Trans. A*, *30*, 127–132.

Imayama, T., T. Takeshita, and K. Arita (2010), Metamorphic P-T profile and P-T path discontinuity across the far-eastern Nepal Himalaya: Investigation of channel flow models, *J. Metamorph. Geol.*, *28*, 527–549, doi:10.1111/j.1525-1314.2010.00879.x.

Inger, S., and N. B. W. Harris (1992), Tectonothermal evolution of High Himalayan Crystalline Sequence, Langtang Valley, Nepal, *J. Metamorph. Geol.*, *10*, 439–452, doi:10.1111/j.1525-1314.1992.tb00095.x.

Inger, S., and N. Harris (1993), Geochemical Constraints on Leucogranite Magmatism in the Langtang Valley, Nepal Himalaya, *J. Petrol.*, *34*, 345–368.

Jamieson, R. A., C. Beaumont, J. Hamilton, and P. Fullsack (1996), Tectonic assembly of inverted metamorphic sequences, *Geology*, *24*, 839–842, doi:10.1130/0091-7613(1996)024<0839:TAOIMS>2.3.CO;2.

Jamieson, R. A., C. Beaumont, S. Medvedev, and M. H. Nguyen (2004), Crustal channel-flows: 2. Numerical models with implcations for metamorphism in the Himalayan-Tibetan orogen, *J. Geophys. Res.*, *109*, B06407, doi:10.1029/2003JB002811.

Jamieson, R. A., C. Beaumont, M. H. Nguyen, and D. Grujic (2006), Provenance of the GHS and associated rocks: Predictions of channel flow models, in *Channel Flow, Ductile Extrusion and Exhumation in Continental Collision Zones*, edited by R. D. Law, M. P. Searle, and L. Godin, *Geol. Soc. Spec. Publ.*, *268*, 165–182.

Janda, C., C. Hager, B. Grasemann, E. Draganits, J.-C. Vannay, B. Bookhagen, and R. Thiede (2002), The Karcham normal fault: Implications for an active extruding wedge, Sutlej Valley, NW Himalaya, *J. Asian Earth Sci.*, *20*, 19–20.

Jessup, M. J., D. L. Newell, J. M. Cottle, A. L. Berger, and J. A. Spotila (2008), Orogen-parallel extension and exhumation enhanced by denudation in the trans- Himalayan Arun River gorge, Ama Drime Massif, Tibet-Nepal, *Geology*, *36*, 587–590, doi:10.1130/G24722A.1.

Kacker, A. K., and M. C. Srivastava (1996), Redlichia from Milam Formation of Martoli Group, Kumaon Himalaya, India—Systematics and significance: Proceedings of Symposium on Recent Advances in Geological Studies of Northwest Himalaya and the Foredeep, *Spec. Publ. Ser. Geol. Surv. India*, *21*, 291–293.

Kali, E., P. H. Leloup, N. Arnaud, G. Mahéo, D. Liu, E. Boutonnet, J. VanderWoerd, L. Xiaohan, J. Liu-Zeng, and L. Haibing (2010), Exhumation history of the deepest central Himalayan rocks (Ama Drime range): Key P-T-D-t constraints on orogenic models, *Tectonics*, *29*, TC2014, doi:10.1029/2009TC002551.

Kanungo, D. N., and D. S. N. Murthy (1981), Structures in the Tethys Himalayas and their Tectonic Significance, *J. Geol. Soc. India*, *22*, 357–367.

Kellett, D. A., and L. Godin (2009), Pre-Miocene deformation of the Himalayan superstructure, Hidden valley, central Nepal, *J. Geol. Soc.*, *166*, 261–275, doi:10.1144/0016-76492008-097.

Kohn, M. J. (2003), Geochemical zoning in metamorphic minerals, in *Treatise on Geochemistry*, vol. 3, *The Crust*, edited by R. Rudnick, pp. 229–261, Elsevier, Amsterdam.

Kohn, M. J. (2008), P-T-t data from central Nepal support critical taper and repudiate large-scale channel flow of the GHS, *Geol. Soc. Am. Bull.*, *120*, 259–273, doi:10.1130/B26252.1.

Kohn, M. J., and F. S. Spear (1991), Error propagation for barometers. 2, Application to rocks, *Am. Mineral.*, *76*, 138–147.

Kohn, M. J., and F. Spear (2000), Retrograde net transfer reaction insurance for pressure-temperature estimates, *Geology*, *28*, 1127–1130, doi:10.1130/0091-7613(2000)28<1127:RNTRIF>2.0.CO;2.

Kohn, M. J., M. S. Wieland, C. D. Parkinson, and B. N. Upreti (2005), Five generations of monazite in Langtang gneisses: Implications for chronology of the Himalayan metamorphic core, *J. Metamorph. Geol.*, *23*, 399–406, doi:10.1111/j.1525-1314.2005.00584.x.

Koziol, A. M. (1989), Recalibration of the garnet-plagioclase: Al2SiO5-quartz (GASP) geobarometer and applications to natural parageneses, *Eos Trans. AGU*, *70*, 493.

Koziol, A. M., and R. C. Newton (1988), Redetermination of the anorthite breakdown reaction and improvement of the plagioclase-garnet-Al2SiO5-quartz geobarometer, *Am. Mineral.*, *73*, 216–223.

Koziol, A. M., and R. C. Newton (1989), The activity of grossular in ternary (Ca,Fe,Mg) garnet determined by reversed phase equilibrium experiments at 1000°C and 900°C, *Contrib. Mineral. Petrol.*, *103*, 423–433, doi:10.1007/BF01041750.

Kruhl, J. H. (1996), Prism- and basal-plane parallel subgrain boundaries in quartz: A microstructural geothermobarometer, *J. Metamorph. Geol.*, *14*, 581–589, doi:10.1046/j.1525-1314.1996.00413.x.

Langille, J. M., M. J. Jessup, J. M. Cottle, D. Newell, and G. Seward (2010), Kinematic evolution of the Ama Drime detachment: Insights into orogen-parallel extension and exhumation of the Ama Drime Massif, Tibet-Nepal, *J. Struct. Geol.*, *32*, 900–919, doi:10.1016/j.jsg.2010.04.005.

Larson, K. P., L. Godin, and R. A. Price (2010), Kinematic compatibility in orogens: Linking the Himalayan foreland and hinterland in central Nepal, *Geol. Soc. Am. Bull.*, *122*, 1116–1134, doi:10.1130/B30073.1.

Le Fort, P. (1975), Himalaya, the collided range: Present knowledge of the continental arc, *Am. J. Sci.*, *275A*, 1–44.

Long, S., and N. McQuarrie (2010), Placing limits on channel-flow: Insights from the Bhutan Himalaya, *Earth Planet. Sci. Lett.*, *290*, 375–390, doi:10.1016/j.epsl.2009.12.033.

Macfarlane, A. M. (1995), An evaluation of the inverted metamorphic gradient at Langtang National Park, Central Nepal, Himalaya, *J. Metamorph. Geol.*, *13*, 595–612, doi:10.1111/j.1525-1314.1995.tb00245.x.

Macfarlane, A. M., K. V. Hodges, and D. Lux (1992), A structural analysis of the main Central thrust zone, Langtang National Park, central Nepal Himalaya, *Geol. Soc. Am. Bull.*, *104*, 1389–1402, doi:10.1130/0016-7606(1992)104<1389:ASAOTM>2.3.CO;2.

Mainprice, D. H., J. L. Bouchez, P. Blumenfeld, and J. M. Tubia (1986), Dominant c slip in naturally-deformed quartz: Implications for dramatic plastic softening at high temperature, *Geology*, *14*, 819–822, doi:10.1130/0091-7613(1986)14<819:DCSIND>2.0.CO;2.

Mancktelow, N. S., and G. Pennacchioni (2004), The influence of grain boundary fluids on the microstructure of quartz-feldspar mylonites, *J. Struct. Geol.*, *26*, 47–69, doi:10.1016/S0191-8141(03)00081-6.

Metcalfe, R. P. (1993), Pressure, temperature and time constraints on metamorphism across the MCT zone and High Himalayan Slab in the Garhwal Himalaya, in *Himalayan Tectonics*, edited by P. J. Treloar and M. P. Searle, *Geol. Soc. Spec. Publ.*, *74*, 485–509.

Meyer, M. C., G. Wiesmayr, M. Brauner, H. Hausler, and D. Wangda (2006), Active tectonics in Eastern Lunana (NW Bhutan): Implications for the seismic and glacial hazard potential of the Bhutan Himalaya, *Tectonics*, *25*, TC3001, doi:10.1029/2005TC001858.

Miyazaki, K. (2007), Formation of a high-temperature metamorphic complex due to pervasive melt migration in the hot crust, *Isl. Arc*, *16*, 69–82, doi:10.1111/j.1440-1738.2007.00559.x.

Nabelek, P. I., and M. Liu (2004), Petrologic and thermal constraints on the origin of leucogranites in collisional orogens, *Trans. R. Soc. Edinburgh Earth Sci.*, *95*, 73–85, doi:10.1017/S0263593300000936.

Passchier, C. W., and R. A. J. Trouw (2005), *Microtectonics*, Springer, Berlin.

Paul, S. K. (1998), Geology and tectonics of the Central Crystallines of northeastern Kumaun Himalaya, India, *J. Nepal Geol. Soc.*, *18*, 151–167.

Powell, R., and T. J. B. Holland (1988), An internally consistent thermodynamic dataset with uncertainties and correlations. 3, Applications to geobarometry, worked examples and a computer program, *J. Metamorph. Geol.*, *6*, 173–204, doi:10.1111/j.1525-1314.1988.tb00415.x.

Powell, R., and T. J. B. Holland (1994), OP-Timal geothermometry and geobarometry, *Am. Mineral.*, *79*, 120–133.

Robinson, D. M., and O. N. Pearson (2006), Exhumation of Greater Himalayan rock along the MCT in Nepal: Implications for channel-flow, in *Channel Flow, Ductile Extrusion and Exhumation in Continental Collision Zones*, edited by R. D. Law, M. P. Searle, and L. Godin, *Geol. Soc. Spec. Publ.*, *268*, 255–267.

Robinson, D. M., P. G. DeCelles, and P. Copeland (2006), Tectonic evolution of the Himalayan thrust belt in western Nepal: Implications for channel-flow models, *Geol. Soc. Am. Bull.*, *118*, 865–885, doi:10.1130/B25911.1.

Sachan, H. K., M. J. Kohn, A. Saxena, and S. L. Corrie (2010), The Malari leucogranite, Garhwal Himalaya, northern India: Chemistry, age, and tectonic implications, *Geol. Soc. Am. Bull.*, *122*, 1865–1876, doi:10.1130/B30153.1.

Searle, M. P. (1999), Emplacement of Himalayan leucogranites by magma injection along giant sill complexes: Examples from the Cho Oyu, Gyachung Kang and Everest leucogranites (Nepal Himalaya), *J. Asian Earth Sci.*, *17*, 773–783, doi:10.1016/S1367-9120(99)00020-6.

Searle, M. P. (2010), Low-angle normal faults in the compressional Himalayan orogen; Evidence from the Annapurna-Dhaulagiri Himalaya, Nepal, *Geosphere*, *6*, 296–315, doi:10.1130/GES00549.1.

Searle, M. P., and L. Godin (2003), The South Tibetan Detachment and the Manaslu Leucogranite: A Structural Reinterpretation and Restoration of the Annapurna-Manaslu Himalaya, Nepal, *J. Geol.*, *111*, 505–523, doi:10.1086/376763.

Searle, M. P., R. R. Parrish, K. V. Hodges, A. Hurford, M. W. Ayres, and M. J. Whitehouse (1997), Shisha Pangma Leucogranite, South Tibetan Himalaya: Field relations, geochemistry, age, origin, and emplacement, *J. Geol.*, *105*, 295–318, doi:10.1086/515924.

Simpson, C., and R. P. Wintsch (1989), Evidence for deformation-induced K-feldspar replacement by myrmekite, *J. Metamorph. Geol.*, *7*, 261–275, doi:10.1111/j.1525-1314.1989.tb00588.x.

Singh, S., P. K. Mukherjee, A. K. Jain, P. P. Khanna, N. K. Saini, and R. Kumar (2003), Source characterization and possible emplacement mechanism of collision-related Gangotri Leucogranite along Bhagirathi Valley, NW-Himalaya, *J. Virtual Explorer*, *11*, 15–26, doi:10.3809/jvirtex.2003.00067.

Smellie, J. A. T. (1974), Formation of atoll garnets from the aureole of the Ardara pluton, Co. Donegal, Ireland, *Mineral. Mag.*, *39*, 878–888, doi:10.1180/minmag.1974.039.308.07.

Spear, F. S. (1993), *Metamorphic Phase Equilibria and Pressure-Temperature-Time Paths*, 799 pp., Mineral. Soc. of Am., Washington, D. C.

Spear, F. S., and J. T. Cheney (1989), A petrogenetic grid for pelitic schists in the system SiO2–Al2O3–FeO–MgO–K2O–H2O, *Contrib. Mineral. Petrol.*, *101*, 149–164, doi:10.1007/BF00375302.

Spear, F. S., J. Selverstone, D. Hickmott, P. Crowley, and K. V. Hodges (1984), P-T paths from garnet zoning. a new technique for deciphering tectonic processes in crystalline terranes, *Geology*, *12*, 87–90, doi:10.1130/0091-7613(1984)12<87:PPFGZA>2.0.CO;2.

Spear, F. S., S. M. Peacock, M. J. Kohn, F. P. Florence, and T. Menard (1991), Computer programs for petrologic P-T-t path calculations, *Am. Mineral.*, *76*, 2009–2012.

Spear, F. S., M. J. Kohn, and J. T. Cheney (1999), P-T paths from anatectic pelites, *Contrib. Mineral. Petrol.*, *134*, 17–32, doi:10.1007/s004100050466.

Stipp, M., H. Stunitz, R. Heilbronner, and S. M. Schmid (2002), The eastern Tonale fault zone: A 'natural laboratory' for crystal plastic deformation over a temperature range from 250 to 700 °C, *J. Struct. Geol.*, *24*, 1861–1884, doi:10.1016/S0191-8141(02)00035-4.

Thiede, R. C., B. Bookhagen, J. R. Arrowsmith, E. R. Sobel, and M. R. Strecker (2004), Climatic control on rapid exhumation along the Southern Himalayan Front, *Earth Planet. Sci. Lett.*, *222*, 791–806, doi:10.1016/j.epsl.2004.03.015.

Valdiya, K. S. (1978), Outline of the structure of the Kumaun Himalaya, in *Tectonic Geology of the Himalaya*, edited by P. S. Saklani, pp. 1–14, Today and Tomorrow's Publ., New Delhi.

Valdiya, K. S. (1979), An outline of the structtural set-up of the Kumaun Himalaya, *J. Geol. Soc. India*, *20*, 145–157.

Valdiya, K. S. (1980), *Geology of Kumaun Lesser Himalaya*, 291 pp., Wadia Inst. of Himalayan Geol, Dehradun, India.

Valdiya, K. S. (1989), Trans-Himadri intracrustal fault and basement upwarps south of Indus-Tsangpo suture zone, in *Tectonics of Western Himalayas*, edited by L. L. Malinconico and R. J. Lillie, *Spec. Pap. Geol. Soc. Am.*, *232*, 153–168.

Valdiya, K. S., S. K. Paul, T. Chandra, S. S. Bhakuni, and R. C. Upadhyaya (1999), Tectonic and lithological characterization of Himadri (Great Himalaya) between Kali and Yamuna rivers, Central Himalaya, *Himal. Geol.*, *20*, 1–17.

Vannay, J. C., and B. Grasemann (2001), Himalayan inverted metamorphism and syn-convergence extension as a consequence ofa general shear extrusion, *Geol. Mag.*, *138*, 253–276, doi:10.1017/S0016756801005313.

Vannay, J.-C., and K. V. Hodges (1996), Tectonometamorphic evolution of the Himalayan metamorphic core between Annapurna and Dhaulagiri, central Nepal, *J. Metamorph. Geol.*, *14*, 635–656, doi:10.1046/j.1525-1314.1996.00426.x.

Vannay, J. C., Z. D. Sharp, and B. Grasemann (1999), Himalayan inverted metamorphism constrained by oxygen isotope thermometry, *Contrib. Mineral. Petrol.*, *137*, 90–101, doi:10.1007/s004100050584.

Vannay, J. C., B. Grasemann, M. Rahn, W. Frank, A. Carter, V. Baudraz, and M. Cosca (2004), Miocene to Holocene exhumation of

metamorphic crustal wedges in the NW Himalaya: Evidence for tectonic extrusion coupled to fluvial erosion, *Tectonics*, *23*, TC1014, doi:10.1029/2002TC001429.

Vidal, P., A. Cocherie, and P. Le Fort (1982), Geochemical investigations of the origin of the Manaslu leucogranite (Himalay, Nepal), *Geochim. Cosmochim. Acta*, *46*, 2279–2292, doi:10.1016/0016-7037(82)90201-0.

Virdi, N. S. (1986), Indus-Tsangpo suture in the Himalaya-crustal expression of a palaeo-subduction zone, *Ann. Soc. Geol. Pol.*, *56*, 3–31.

Webb, A. A. G., A. Yin, T. M. Harrison, J. Célérier, and W. P. Burgress (2007), The leading edge of the Greater Himalayan Crystalline complex revealed in the NW Indian Himalaya. Implications for the evolution of the Himalayan orogen. *Geology*, *35*, 955–958, doi:10.1130/G23931A.1.

Yin, A. (2006), Cenozoic tectonic evolution of the Himalayan orogen as constrained by along-strike variation in structural geometry, exhumation history, and foreland sedimentation, *Earth Sci. Rev.*, *76*, 1–131, doi:10.1016/j.earscirev.2005.05.004.

M. J. Dorais and R. A. Harris, Department of Geological Sciences, Brigham Young University, Provo, UT 84602, USA.

C. J. Spencer, Department of Earth Sciences, University of St Andrews, St Andrews KY16 9AJ, UK. (cs207@st-andrews.ac.uk)